CHALMERS
UNIVERSITY OF TECHNOLOGY

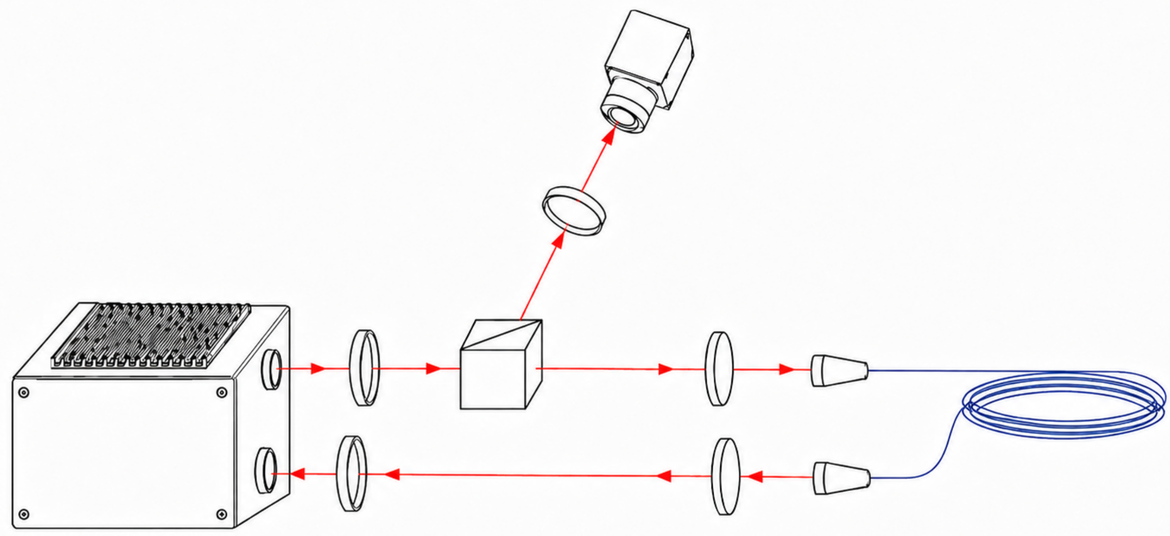

Fiber-Based Indoor Testing of Laser Rangefinder Extinction Ratio

Development, Characterization, and Evaluation of a Laboratory Test Bench as an Alternative to Outdoor Over-the-Air Testing

Master's thesis in Physics

LINUS BRINK

DEPARTMENT OF MICROTECHNOLOGY AND NANOSCIENCE

CHALMERS UNIVERSITY OF TECHNOLOGY
Gothenburg, Sweden 2026
www.chalmers.se

Master's thesis 2026

Fiber-Based Indoor Testing of Laser Rangefinder Extinction Ratio

Development, Characterization, and Evaluation of a Laboratory Test Bench as an Alternative to Outdoor Over-the-Air Testing

LINUS BRINK

Department of Microtechnology and Nanoscience
Division of Photonics
Chalmers University of Technology
Gothenburg, Sweden 2026

Fiber-Based Indoor Testing of Laser Rangefinder Extinction Ratio
Development, Characterization, and Evaluation of a Laboratory Test Bench as an Alternative to Outdoor Over-the-Air Testing
LINUS BRINK

Technical Supervisor: Robin Sandström, Lumibird Photonics Sweden AB
Responsible Supervisor: Stefan Horrdin, Lumibird Photonics Sweden AB
Examiner: Åsa Haglund, Department of Microtechnology and Nanoscience

Master's Thesis 2026
Department of Microtechnology and Nanoscience
Division of Photonics
Chalmers University of Technology
SE-412 96 Gothenburg
Telephone +46 31 772 1000

Cover: Simplified schematic illustration of the fiber-based indoor testing concept for evaluating laser rangefinder extinction ratio.

Typeset in LaTeX
Printed by Chalmers Reproservice
Gothenburg, Sweden 2026

Fiber-Based Indoor Testing of Laser Rangefinder Extinction Ratio
Development, Characterization, and Evaluation of a Laboratory Test Bench as an Alternative to Outdoor Over-the-Air Testing
LINUS BRINK
Department of Microtechnology and Nanoscience
Chalmers University of Technology

Abstract

Laser rangefinders (LRFs) are one of the most prominent optronic systems used for both civilian and military applications. One way to characterize their performance is by measuring the extinction ratio (ER), defined as the attenuation at which the LRF detects 50 % of the transmitted pulses. At Lumibird Photonics Sweden AB, the ER is currently determined using an outdoor over-the-air (OTA) test range, where the laser pulse is fired at a well-defined reference target. To eliminate the weather dependence inherent to outdoor OTA testing, this thesis investigates an indoor laboratory test bench using a single-mode fiber to guide the pulses as an alternative ER measurement method. The work focused on establishing stable free-space-to-fiber coupling, selecting a suitable baseline attenuation before fiber injection, and comparing the ER behavior with an OTA reference measurement.

Using a deliberately larger focused beam at the fiber input reduced the influence of pulse-to-pulse beam variations on the coupling efficiency. In addition, nonlinear propagation in the fiber was found to be the main limitation on the maximum usable coupled intensity, causing pulse distortion when it was too high. With suitable baseline attenuation, the final test bench produced a clear detection roll-off similar to the OTA reference. The test-bench ER was obtained at ≈ 101 dB of added attenuation, and the measured distance agreed with the expected fiber-delay distance within ≈ 1 %. Including estimated setup-specific losses, the same 50 % detection point corresponded to a test-bench total attenuation of ≈ 110 dB, compared with ≈ 130 dB for the OTA reference, with the difference likely arising from idealized assumptions regarding losses in the test bench.

Overall, the test bench shows potential as an indoor complement to OTA ER testing, but further characterization of losses, repeatability, and uncertainty is required before it can be used for final performance evaluation.

Keywords: laser rangefinder, extinction ratio, test bench, single-mode fiber, fiber coupling

Acknowledgements

I would like to sincerely thank Lumibird Photonics Sweden AB and my responsible supervisor, Stefan Horrdin, who entrusted me with the opportunity to carry out this thesis work. It has been a very interesting project with many rewarding challenges, discussions, and analyses, as well as an incredibly valuable learning experience. I am especially grateful to my technical supervisor, Robin Sandström, for his guidance, support, and encouragement throughout the project, without which I would not have been able to get as far as I did. I would also like to thank Hugo Söderberg for his interest in the thesis and his many helpful insights. My thanks also go to Stellan Wickström for his assistance in the early stages of the project, as well as anyone else who had an impact on the thesis in any way.

Finally, I would like to express my gratitude to my examiner on Chalmers, Åsa Haglund, who believed in me and accepted my thesis work on very short notice, despite an already busy schedule. I am very thankful for her support throughout the project, both with the work itself and with everything around it.

Linus Brink, Gothenburg, June 2026

List of Acronyms

Below is the list of acronyms that have been used throughout this thesis listed in alphabetical order:

CW	Continuous Wave
ER	Extinction Ratio
FWHM	Full Width of Half Maximum
GRIN	Graded-Index
LPS	Lumibird Photonics Sweden AB
LRF	Laser Rangefinder
MFD	Mode Field Diameter
MMF	Step-Index Multimode Fiber
NA	Numerical Aperture
OTA	Over the Air
PRF	Pulse Repetition Frequency
SBS	Stimulated Brillouin Scattering
SMF	Single-Mode Fiber
SRS	Stimulated Raman Scattering
TIR	Total Internal Reflection
TOF	Time of Flight
TVG	Time Variable Gain
VOA	Variable Optical Attenuator

Nomenclature

The following Nomenclature lsits the main symbols used throughout this thesis. The symbols are grouped according to the theoretical or experimental context in which they are primarily used.

LRF Principles and Attenuation

A	Attenuation
A_{tot}	Total attenuation
c	Speed of light in vacuum
N	LRF internal timing circuit clock counts
P_{in}	Power before transmission
P_{out}	Power after transmission
P_{ref}	Reference received optical power
P_{th}	Minimum received optical power for detection
S	Range to target determined by the LRF
S_0	Reference target distance for the OTA ER acceptance configuration
S_1	Actual target distance for the OTA ER test range
T	Transmission factor
T_{A}	One-way atmospheric transmission factor to a target
T_{clk}	LRF internal timing circuit clock period
T_{tot}	Total transmission factor
ρ	Target reflectivity
ρ_0	Reference target reflectivity for the OTA ER acceptance configuration
ρ_1	Actual target reflectivity for the OTA ER test range

Gaussian Optics

f	Focal length
I	Optical intensity
$I(r, z)$	Spatial intensity at the temporal pulse peak
$P(t)$	Instantaneous power
P_{peak}	Temporal pulse peak power
r	Radial distance
$r_{\text{enc}}(z)$	Aperture radius enclosing the power or energy fraction T at axial position
$R(z)$	Wavefront radius of curvature
R_{lens}	Radius of curvature of a lens surface
t	Time
W	Collimated e^{-2} beam radius at the focusing lens
$w(z)$	e^{-2} beam radius at axial position z
w_0	e^{-2} waist radius of the incident beam
w_{f}	Focused e^{-2} waist radius
z	Axial propagation coordinate relative to the beam waist
z_{R}	Rayleigh range
λ	Wavelength in the propagation medium
τ	Pulse duration
τ_{FWHM}	Full width at half maximum pulse duration
θ_{div}	e^{-2} half-angle divergence
θ_{enc}	Half-angle divergence corresponding to an encircled power or energy fraction

Fiber Optics and Coupling

a	Fiber core radius
d	Lateral offset between the beam center and the fiber mode center
k_0	Vacuum wavenumber
L	Fiber length
MFD	Fiber mode field diameter
NA	Numerical aperture of the fiber
n	Refractive index
n_0	Refractive index of the external launch medium
$n(r)$	Radially dependent refractive index
n_{clad}	Fiber cladding refractive index

n_{core}	Fiber core refractive index
n_{g}	Group index of a guided mode
P_{a}	Available incident power
P_{c}	Coupled guided power
q	Focused-beam to mode-field radius ratio, defined as $w_{\text{f}}/w_{\text{MFD}}$
t_{g}	Group delay through a fiber
V	Normalized frequency, usually referred to as the fiber parameter
v_{g}	Group velocity of a pulse in a fiber
w_{MFD}	Mode field radius, defined as MFD/2
β	Axial propagation constant of a guided fiber mode
η	Free-space–to–fiber coupling efficiency
λ_0	Wavelength in vacuum
θ_{a}	Acceptance half-angle within which launched light can be guided by the fiber
θ_{c}	Critical angle for total internal reflection at the fiber core–cladding interface

Nonlinear Effects

g_{B}	Brillouin gain coefficient
$I_0(\cdot)$	Zeroth-order modified Bessel function
I_{th}	SBS threshold intensity
n_2	Nonlinear refractive-index coefficient
n_{lin}	Linear refractive index
T_{B}	Acoustic phonon lifetime
γ	Dimensionless SBS intensity parameter
$\Delta\nu_{\text{B}}$	Brillouin gain linewidth
$\Delta\nu_{\text{B,eff}}$	Effective Brillouin gain linewidth for pulsed operation
Θ	Dimensionless SBS threshold parameter
Λ	Dimensionless SBS fiber length parameter
$\bar{\tau}$	Dimensionless SBS pulse-duration parameter

Measurements and Data Processing

c_l	Left-side interpolated half-maximum crossing point
c_r	Right-side interpolated half-maximum crossing point

x	Transverse horizontal coordinate
x_i	Time coordinate of sampled pulse point i
x_c	Estimated effective horizontal coupling-center coordinate
x_f	Horizontal focal-plane centroid coordinate
$\tilde{x}_\mathrm{f}$	Median horizontal focal-plane centroid coordinate
y	Transverse vertical coordinate
y_i	Signal value of sampled pulse point i
y_c	Estimated effective vertical coupling-center coordinate
y_f	Vertical focal-plane centroid coordinate
$\tilde{y}_\mathrm{f}$	Median vertical focal-plane centroid coordinate
y_max	Peak pulse signal value
z_stage	Translation-stage axial position relative to the foremost stage position
$\lvert\alpha\rvert$	Relative pointing magnitude
α_x	Relative horizontal pointing angle
α_y	Relative vertical pointing angle
Δx	Horizontal displacement relative to x_c
Δy	Vertical displacement relative to y_c

Contents

List of Figures

List of Tables

1

Introduction

This chapter presents the outline of the thesis project. It includes a background to why it is conducted, prior work, and the aim of the thesis with objectives and limitations. It also includes a section on societal, ethical, and ecological aspects.

1.1 Background

Laser rangefinders (LRFs) are a constantly evolving technology that originates from the 1960s [1], and is currently one of the most prominent types of optronic systems in various applications, both civilian and military [2].

Lumibird, with its 25 years of experience, is one of the leading global specialists in the developing and manufacturing of lasers for scientific, industrial, and medical applications [3]. In 2022, Lumibird acquired Saab's defense LRF business in Gothenburg, Sweden with a 60 year history of expertise in manufacturing LRFs. The now Lumibird Photonics Sweden AB (LPS) specializes in LRFs for military land, naval, and airborne applications [4].

Most common LRFs, including those manufactured by LPS, function based on the so-called time-of-flight (TOF) method. The TOF method determines the distance to a target by accounting for the speed of light in air and measuring the time it takes a fired laser pulse to make a round-trip to and from the target [1].

A common but crucial parameter to assess range capabilities of an LRF is the extinction ratio (ER), which determines the maximum optical attenuation that can be put in the LRF path for it to still function as intended [2]. A common way to do this test is with an over-the-air (OTA) measurement [2], which is also the method currently used at LPS [5]. An OTA measurement is essentially a field test, where the LRF is aimed at a reference target with a certain reflectivity positioned at a known distance under the prevailing atmospheric conditions [2], [5]. An increasing amount of attenuation is put in the LRF path until the ER is reached. The achieved ER value is compared to a reference acceptance value for which the LRF is considered to function properly. This value is defined on a specific reference configuration with well-defined conditions.

The problem with OTA tests is that the outcome of the test strongly depends on the exact weather at the time of the measurement since atmospheric conditions affects the attenuation. The OTA tests at LPS assume 100 % transmission at all times [5], since a reliable representation of the actual transmission is not currently possible and therefore can not be communicated with confidence to the customer. This results in the LRF OTA ER performance measurements only being possible if the visibility is $> 2\,\text{km}$ [5]. LPS therefore wants a way to be able to run the ER tests in an indoor laboratory environment, where the weather will not influence the measurements.

1.2 Project Context and Solutions on the Market

A pre-study on potential solutions for an indoor test was carried out by Théo Mingant during the spring and summer of 2025 [6]. Mingant [6] proposed two potential avenues to performing the ER measurement in a laboratory environment. The first uses a fiber to resemble the distance of the OTA measurement, and the second a laser diode and power meter to simulate the reflection by interpreting the transmitted pulse and sending out a new pulse with a controlled time delay.

There are commercial solutions utilizing the two ideas proposed by T. Mingant [6]. Among these are Inframet's LTF (fiber) and LUNI (signal simulation) test stations, which enable measurement of the ER ratio together with several other parameters [7], [8]. However, these test stations are associated with higher upfront costs and reduced flexibility due to dependence on an external manufacturer. Developing an internal solution requires a greater initial time and work investment, but offers more adaptability to specific testing requirements. This is especially beneficial when developing various types of LRFs with different configurations and is also important when working with military information.

The fiber-based approach was considered the more viable option, mostly because of its real optical propagation over a physical path length. Based on this conclusion, the optical components required for the proposed setup were procured in 2025. A simpler version of the test bench was created to test the coupling of the laser into the fiber, but no signal could be detected at the fiber output.

1.3 Aim

The aim of this thesis is to investigate, develop, and evaluate the limitations of a test bench for carrying out ER measurements of LRFs in an indoor laboratory environment. This allows LRF behavior verification during the development process and final performance testing prior to customer delivery, independent of weather conditions.

1.4 Objectives

In order to carry out the work and fulfill its purpose, the process is divided into multiple objectives. These objectives are:

- Quantify the attenuation and splitting ratios of filters and beam splitters used in the optical path.
- Establish free-space–to–fiber coupling of the LRF pulses and detect the transmitted signal.

- Determine a baseline attenuation required to prevent damage and nonlinear pulse distortion in the fiber link.
- Evaluate pulse-to-pulse coupling stability and identify beam parameters affecting the free-space–to–fiber coupling.
- Perform ER measurements on the indoor test bench and analyze the range determination.
- Compare the ER behavior of the test bench with an OTA reference measurement and evaluate the limitations of the test bench.

1.5 Delimitations

To ensure that the project remains manageable and that clear conclusions can be drawn, specific delimitations are set. The test bench is configured for LRFs with spatially separated transmitter and receiver openings, meaning that interference between outgoing and incoming pulses is not considered. More specifically, the optics are optimized for the LPS Heimdall LRF, since units are available and because it uses similar technology to the prominent LPS VIDAR LRF. The setup is also limited to simulating the distance to a single target, although the LRF itself is capable of measuring two targets simultaneously.

The project is constrained to the single-mode fiber (SMF) architecture and the corresponding fiber-link components procured in 2025. Possible alternatives to the selected fiber type are discussed, but are not experimentally evaluated. Optical output characteristics of the LRF, such as beam diameter and divergence, are assumed to be within the product specifications prior to ER measurements.

1.6 Societal, Ethical, and Ecological Aspects

The engineering profession is directly responsible for public quality of life and protecting the environment [9]. General public trust is required, which means engineers are held to high ethical standards. It is therefore important to consider the societal, ethical, and ecological aspects related to the thesis during the project.

LPS develops and manufactures LRFs for defense industry applications [4]. The LRFs themselves are eye-safe and not dangerous, but their appliance is partly in weapon systems that are. National Society of Professional Engineers [9] specifically states to “hold paramount the safety, health, and welfare of the public” as one of the fundamental canons of the engineering profession. Whether work in the defense industry aligns with this principle is subject to debate [10]. The justification for developing weapon systems is deterrence and, in the worst case, direct defense against threats to society, democracy, and territorial integrity [11]. However, these systems also have the capacity to cause severe harm to people and the environment. To reduce risks of system misuse, the export of military equipment is restricted under Swedish law [12].

The general purpose of this thesis is to investigate and construct a test bench for LRFs in an indoor laboratory environment. This to eliminate the atmospheric testing parameter and be able to test the LRFs independent on weather conditions. This means that the thesis itself is not a determining part in the manufacturing of these LRFs, but it can potentially lead to more efficient testing and therefore accelerated customer delivery in the future. The thesis primarily used products that were already procured or are needed in the laboratory anyway, and thus has little effect on the environment.

Since the project method does not pose a direct risk to others, the potentially negative implications of the work being minor, parts used are mostly already in stock, and LPS being required to operate under Swedish law, it is not considered to cause any significant societal, ethical, or ecological issues.

1.7 Thesis Outline

This master's thesis consists of six chapters. Chap. 1 introduces the work by providing the necessary context and relevant prior background. It also presents the aim of the thesis, including its objectives and delimitations. In addition, the societal, ethical, and ecological aspects are discussed.

Chap. 2 outlines the theory required to understand the method, results, and discussion. This includes information on LRFs, ER, and general Gaussian optics, as well as fiber optics, including fiber types, the principles of fiber light propagation, and coupling efficiency. Stimulated Brillouin scattering (SBS) and other fiber nonlinearities are also described.

The methods used to fulfill the aim of the thesis and reach a satisfactory conclusion are presented in Chap. 3. These include determining the baseline attenuation needed to prevent damage and nonlinearities as well as studying pulse-to-pulse effects on the coupling-efficiency. The ER testing approach for both the OTA and indoor test bench configurations are also presented as well as the test bench configuration including construction and alignment of it.

Chap. 4 consists of the results from tests performed based on the methods in Chap. 3. These include the determined baseline attenuation, the LRF pulse-to-pulse influence on coupling efficiency, OTA ER test reference, and ER determination of the test bench.

The results, their significance, and possible future work as well as uncertainties are discussed in Chap. 5. This includes comparing with literature and other experiments performed in earlier papers. Finally, Chap. 6 summarizes the project and presents a conclusion to the thesis.

2

Theory

This chapter provides the necessary theory required to understand the thesis and interpret the results. It includes information about the principles of Laser Rangefinders, ER, Gaussian pulses, and Fiber optics, including light propagation and guiding, the most common fiber types and their characteristics, coupling efficiency from free-space, as well as Stimulated Brillouin Scattering (SBS) and other fiber nonlinearities.

2.1 The Principles of Laser Rangefinders (LRFs)

Most common LRFs function based on TOF [1]. The laser source emits a pulse through transmitter optics, which collimates the beam to a specific divergence and diameter, while simultaneously triggering an internal timing circuit with clock period T_{clk} [1], [13]. The pulse propagates at the speed of light in air c and reflects off a target. A part of the reflected pulse, often called the echo pulse, reaches the receiver, which filters out unwanted wavelengths and focuses the echo signal onto a detector. The detector output is amplified and compared to a specified threshold. When the threshold is exceeded, the internal timing circuit is stopped and the range S is determined by

$$S = \frac{1}{2} c N T_{\text{clk}}, \tag{2.1}$$

where N is the number of clock counts reached during the round-trip.

To prevent false range detection from backscattering on particles in the atmosphere, the LRF has a time variable gain (TVG) filter [14]. The TVG functions like a time-dependent attenuation that applies an initial damping that decreases with time, reducing initial detector sensitivity when the power of the signal is strongest, and increases it as the pulse propagates to be able to detect reflections off targets at great distances.

2.2 Extinction Ratio (ER)

Determining the ER is a way to characterize the range performance of LRFs. ER is expressed in dB and is defined as

$$\text{ER} = 10 \log_{10} \left(\frac{P_{\text{ref}}}{P_{\text{th}}} \right), \tag{2.2}$$

where P_{ref} is the reference received optical power at the detector, and P_{th} the minimum received power required for detection [15].

In practice, the ER corresponds to the total attenuation inserted with optical density filters until the LRF just meets a specified performance criterion, commonly 50 % detection probability [14], [15].

In this context, an attenuation A expressed in dB corresponds to a power transmission factor T through

$$A = -10\log_{10}(T) = 10\log_{10}\left(\frac{P_{\mathrm{in}}}{P_{\mathrm{out}}}\right), \tag{2.3}$$

where P_{in} and P_{out} are the powers before and after transmission respectively [16]. For multiple attenuating elements in series, the transmission factors multiply ($T_{\mathrm{tot}} = \prod_{\mathrm{i}} T_{\mathrm{i}}$), and therefore the attenuations add in dB ($A_{\mathrm{tot}} = \sum_{\mathrm{i}} A_{\mathrm{i}}$).

2.3 Gaussian Optics

The pulses of LRFs are often considered Gaussian in the time domain [13]. The instantaneous power for such a pulse can be written as

$$P(t) = P_{\mathrm{peak}} \exp\left(-4\ln 2\left(\frac{t}{\tau_{\mathrm{FWHM}}}\right)^2\right), \tag{2.4}$$

where P_{peak} is the peak power and τ_{FWHM} the full width at half maximum (FWHM) pulse duration [17]. The pulse energy E_{pulse} can be determined by taking the time integral of $P(t)$, which corresponds to

$$E_{\mathrm{pulse}} = \int_{-\infty}^{\infty} P(t)\,dt = \frac{1}{2}P_{\mathrm{peak}}\tau_{\mathrm{FWHM}}\sqrt{\frac{\pi}{\ln 2}}. \tag{2.5}$$

For pulses that also have a Gaussian transverse spatial profile, its intensity at the temporal pulse peak in cylindrical coordinates is

$$I(r,z) = \frac{2P_{\mathrm{peak}}}{\pi w^2(z)} \exp\left(-2\frac{r^2}{w^2(z)}\right), \tag{2.6}$$

where r and z are the radial and axial propagation coordinate, respectively. $w(z)$ is the Gaussian ISO standard e^{-2} beam radius defined by $I(w(z),z) = e^{-2}I(0,z)$, where $I(0,z)$ is the maximum intensity for any given z

$$I(0,z) = \frac{2P_{\mathrm{peak}}}{\pi w(z)^2}. \tag{2.7}$$

The beam radius is sometimes defined at a certain power level or energy level instead of intensity. This corresponds to the proportion of transmitted power or transmitted energy T within an aperture of radius $r_{\mathrm{enc}}(z)$,

$$T = 1 - \exp\left(-\frac{2r_{\mathrm{enc}}^2(z)}{w^2(z)}\right), \tag{2.8}$$

which can be converted to the e^{-2} radius [18]

$$w(z) = r_{\mathrm{enc}}(z)\sqrt{\frac{2}{-\ln(1-T)}}. \tag{2.9}$$

The same conversion can be done for the e^{-2} divergence. In the far field, sufficiently far from the beam waist, the beam radius increases approximately linearly with propagation distance according to [18], [19]

$$w(z) \approx \theta_{\mathrm{div}} z. \tag{2.10}$$

θ_{div} is the e^{-2} divergence half-angle associated with $w(z)$. Similarly, the radius enclosing the power or energy fraction T increases approximately as

$$r_{\mathrm{enc}}(z) \approx \theta_{\mathrm{enc}} z, \tag{2.11}$$

where θ_{enc} is the half-angle divergence corresponding to this encircled fraction. Inserting Eq. 2.10 and 2.11 into 2.9 gives the e^{-2} divergence half-angle conversion

$$\theta_{\mathrm{div}} = \theta_{\mathrm{enc}} \sqrt{\frac{2}{-\ln(1-T)}}. \tag{2.12}$$

The beam diameter $w(z)$ for a Gaussian beam is determined by [19]

$$w(z) = w_0 \sqrt{1 + \left(\frac{z}{z_R}\right)^2}, \tag{2.13}$$

where w_0 is the minimum beam radius at $z = 0$, called the beam waist, λ is the wavelength in the propagation medium, and z_R the Rayleigh range defined as

$$z_R = \frac{\pi w_0^2}{\lambda}. \tag{2.14}$$

The waist diameter corresponding to the beam waist ($2w_0$) is referred to as the spot size. The beam achieves optimal focus at the waist and the focus gradually decreases as the radius increases in either direction. It is considered to be in focus whenever it is within z_R from the waist and the so-called depth of focus for a beam is therefore defined as $2z_R$. θ_{div} is related to w_0 through the far-field expression

$$\theta_{\mathrm{div}} = \frac{\lambda}{\pi w_0}. \tag{2.15}$$

In addition to its radius, a Gaussian beam is also characterized by its wavefront, defined as a surface of constant optical phase [19]. At the beam waist, the wavefront is planar, while away from the waist it becomes curved. The radius of curvature of the Gaussian beam wavefront is given by

$$R(z) = z \left[1 + \left(\frac{z_R}{z}\right)^2\right], \tag{2.16}$$

where $R(z) \to \infty$ at the waist, corresponding to a planar wavefront. Close to the waist, within approximately one Rayleigh range, the wavefront therefore remains close to planar.

When focusing a Gaussian beam with a focusing lens, the focused beam waist w_f and its axial position relative to the lens focal plane z_{f} are [20]

$$w_{\mathrm{f}} = \frac{w_0 f \theta_{\mathrm{div}}}{\sqrt{w_0^2 + \theta_{\mathrm{div}}^2 z_{\mathrm{L}}^2}} \tag{2.17}$$

and

$$z_{\text{f}} = \frac{z_{\text{L}} f^2}{z_{\text{L}}^2 + \left(\frac{w_0}{\theta_{\text{div}}}\right)^2}, \tag{2.18}$$

where f is the lens focal length and z_{L} the distance from the waist to the lens. For a collimated Gaussian beam with radius W at the convex lens, where W is much larger than both w_f and λ, w_f can be approximated as [21]

$$w_{\text{f}} \approx \frac{\lambda f}{\pi W}. \tag{2.19}$$

f for a lens depends on its curvature radius R_{lens} and the refractive index n of the material it is made out of [22]. For a plano-convex lens, f can be approximated by

$$f = \frac{R_{\text{lens}}}{n-1}. \tag{2.20}$$

Since n is wavelength-dependent, the focal length also depends on λ. This causes different wavelengths to focus at slightly different positions, which is known as chromatic aberration [21], [23]. For a beam with a finite spectral bandwidth, this can cause effective waist broadening.

2.4 Fiber Optics

An optical fiber is a cylindrical dielectric waveguide fabricated from low-loss material [24]. It consists of a core with refractive index n_{core} surrounded by a cladding with index $n_{\text{clad}} < n_{\text{core}}$. The index contrast confines light to the core and allows it to propagate over long distances with low attenuation.

The type of fiber affects coupling tolerance and pulse broadening (dispersion) [24]. Three common fiber types are the step-index multimode fiber (MMF), the single-mode fiber (SMF), and the graded-index (GRIN) MFF. More is presented on these in Sec. 2.4.2–2.4.4.

2.4.1 Light Propagation and Guiding

There are two useful, complementary ways of describing light guidance in fibers [24]. Ray optics provides a simpler, intuitive picture, while electromagnetic wave optics gives the complete description.

In a step-index fiber, the ray picture describes guidance as total internal reflection (TIR) at the core–cladding interface [24]. This is illustrated in Fig. 2.1 and occurs when the incidence angle at the core–cladding boundary exceeds the critical angle θ_{c}, defined by Snell's law as

$$\theta_{\text{c}} = \arcsin\left(\frac{n_{\text{clad}}}{n_{\text{core}}}\right). \tag{2.21}$$

The same guiding condition can also be expressed in terms of how light is launched into the fiber from an external medium with refractive index n_0 [24]. This defines the acceptance half-angle θ_{a}, where rays launched within this cone will refract into the core and still meet the TIR condition at the core–cladding boundary, see Fig. 2.1. The acceptance cone is determined by the numerical aperture

$$\mathrm{NA} = n_0 \sin \theta_\mathrm{a}, \tag{2.22}$$

which for a step-index fiber can be calculated by

$$\mathrm{NA} = \sqrt{n_\mathrm{core}^2 - n_\mathrm{clad}^2}. \tag{2.23}$$

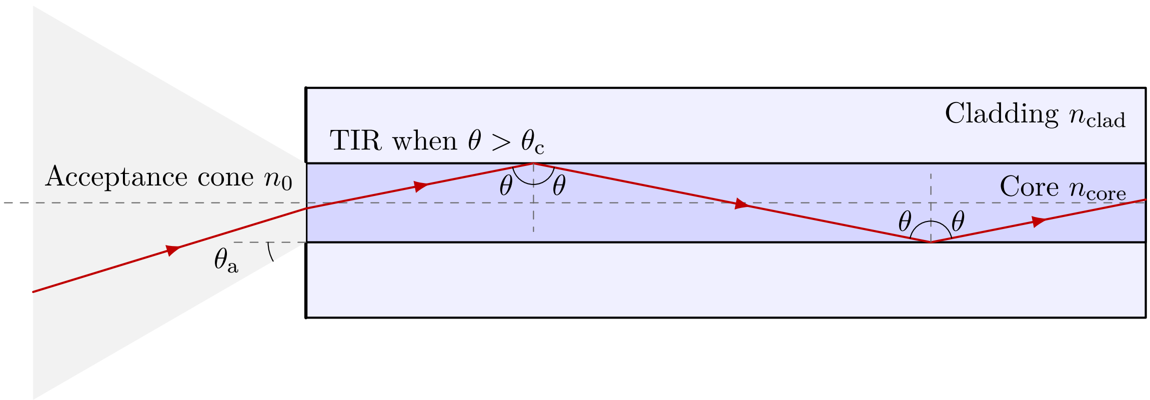

Figure 2.1: A ray-optics schematic illustration of light coupling into a step-index optical fiber. Light entering within the acceptance cone is refracted into the core and guided by TIR at the core–cladding interface. The ray path is displayed in red and the arrows indicate propagation direction. The acceptance cone is shown in lighter gray, while the core and cladding are darker and lighter shades of blue respectively to visualize the higher and lower refractive indices.

A complete description of the light propagation follows from Maxwell's equations where the fiber acts as a cylindrical waveguide that supports a discrete set of guided modes, i.e. distinct solutions to the wave equation that satisfy the electromagnetic boundary conditions at the core–cladding interface [24]. Each mode has a specific transverse field distribution and propagates along the fiber axis as $\exp(i\beta z)$, where β is the mode's propagation constant. For the vacuum wavenumber $k_0 = 2\pi/\lambda_0$, where λ_0 is the wavelength in vacuum, guiding occurs when

$$n_\mathrm{clad} k_0 < \beta < n_\mathrm{core} k_0. \tag{2.24}$$

This condition implies that the field is oscillatory in the core and decays evanescently in the cladding.

A key dimensionless parameter is the normalized frequency, usually referred to as the fiber parameter,

$$V = k_0 a \sqrt{n_\mathrm{core}^2 - n_\mathrm{clad}^2} = \frac{2\pi a}{\lambda_0} \mathrm{NA}, \tag{2.25}$$

where a is the core radius [24]. For step-index fibers, V largely determines how many modes can propagate.

A pulse propagates through a fiber with the group velocity v_g, which describes the velocity of the pulse envelope [25]. It is given by

$$v_g = \frac{c}{n_g}, \tag{2.26}$$

where n_g is the group index of the guided mode. The corresponding transit time t_g for the pulse through a fiber with length L, referred to as the group delay, is

$$t_g = \frac{L}{v_g} = \frac{n_g L}{c}. \tag{2.27}$$

Different propagation effects can broaden the pulse in time as it is guided through the fiber. One contribution is modal dispersion, which occurs because modes have different t_g [24]. This is most easily visualized by imagining multiple rays propagating through the fiber core in different trajectories with different path lengths, causing them to arrive at the end of the fiber at different times, see step-index MMF in Fig. 2.2. A second contribution is chromatic dispersion, which is a consequence of pulses having finite spectral bandwidths and t_g depending on wavelength. This causes different spectral components to arrive at different times, like for the different modes. The effects of chromatic dispersion are significantly smaller compared to modal dispersion.

2.4.2 Step-Index Multimode Fiber (MMF)

A step-index MMF has constant refractive indices in both the core and cladding [24]. Its larger core and typically larger NA make free-space coupling less demanding, since the acceptance angle is larger and the coupling becomes less sensitive to beam size, see Sec. 2.4.5. The main drawback of the step-index MMF is the multiple modes leading to modal dispersion and therefore significant pulse broadening over time. The step-index MMF is illustrated in Fig. 2.2.

2.4.3 Single-Mode Fiber (SMF)

An SMF is designed such that $V < 2.405$, meaning only the fundamental mode propagates, by having a smaller radius and/or NA (see Fig. 2.2) [24]. The distribution of this mode is approximately Gaussian [26] and provides the greatest confinement of light power within the core, resulting in minimum attenuation [24]. Having a single mode also eliminates modal dispersion, significantly reducing pulse broadening over time. The trade-off is stricter coupling requirements because of the smaller core and NA, see Sec. 2.4.5.

The size of the optical field in an SMF is represented by the mode field diameter (MFD), which is approximated by the Marcuse's equation

$$\text{MFD} \approx 2a\left(0.65 + \frac{1.619}{V^{3/2}} + \frac{2.879}{V^6}\right), \tag{2.28}$$

and is typically slightly larger than the core diameter due to the evanescent field in the cladding [26], [27].

2.4.4 Graded-Index (GRIN) Multimode Fiber (MMF)

A GRIN MMF has a core index that decreases gradually with radius $n(r)$ until it reaches a value near n_{clad} at the core boundary [24]. In the ray picture, this causes rays to follow curved trajectories inside the core. The rays traveling farther from the center experience a lower refractive index (higher speed) and can partially compensate for their longer path length. As a result, GRIN MMF can exhibit reduced modal dispersion compared to step-index MMF, while retaining the practical coupling advantages of a larger core compared to the SMF.

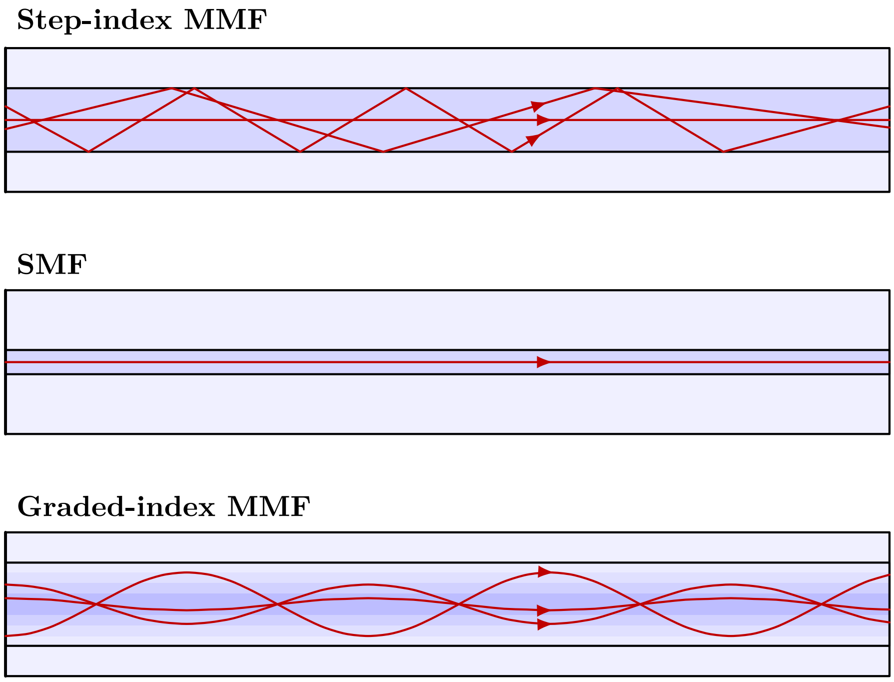

Figure 2.2: Ray-optics schematic comparison of propagation in three optical fiber types, where the darker blue corresponds to the higher refractive index in the core, and the lighter blue the lower index in the cladding. For the graded-index MMF, the color in the core fades from the center to the cladding interface to illustrate the decreasing refractive index. The propagating rays are shown in red, where the arrows indicate direction. In a step-index MMF, multiple modes propagate through TIR. In an SMF, only one fundamental mode propagates, and for a graded-index MMF, the refractive-index profile causes multimode trajectories to follow smooth oscillatory paths.

2.4.5 Free-Space–to–Fiber Coupling Efficiency

The coupling efficiency η is defined as the fraction of available optical power that is launched into guided propagation

$$\eta = \frac{P_{\text{c}}}{P_{\text{a}}}, \tag{2.29}$$

where P_{c} is the coupled (guided) power and P_{a} the available incident power in the coupling system [28], [29].

For an SMF, coupling is fundamentally a mode-matching problem [26], [28]. The coupled power is determined by the overlap between the incident field and the guided fundamental mode. For a Gaussian beam (matching the Gaussian-shaped fundamental mode), η becomes largely alignment-limited [26]. The determining factors become spot-size mismatch, lateral offset, and beam incident angle (tilt).

For an incident Gaussian beam with the waist positioned in the coupling plane of an SMF, assuming negligible tilt, the coupling efficiency is

$$\eta \approx \left(\frac{2w_\mathrm{f} w_\mathrm{MFD}}{w_\mathrm{f}^2 + w_\mathrm{MFD}^2}\right)^2 \exp\left(-\frac{2d^2}{w_\mathrm{f}^2 + w_\mathrm{MFD}^2}\right), \tag{2.30}$$

where w_f is the focused beam e^{-2} radius, d is the lateral offset between the center of the beam and the center of the MFD, and $w_\mathrm{MFD} = \mathrm{MFD}/2$ [26]. The prefactor accounts for spot-size mismatch between w_MFD and w_f, while the exponential factor accounts for lateral offset (visualized in Fig. 2.3). Tilt can be included as an additional exponential reduction factor in the same Gaussian-field overlap model [26]. For sufficiently large tilt, coupling is NA-limited because part of the incident field falls outside the acceptance cone [28].

In practice, efficient SMF coupling also requires the focused waist to be placed at or very close to the fiber endface. As discussed in Sec. 2.3, the wavefront of a Gaussian beam is approximately planar only close to the waist. This helps match the approximately planar phase front of the fiber mode at the endface [20].

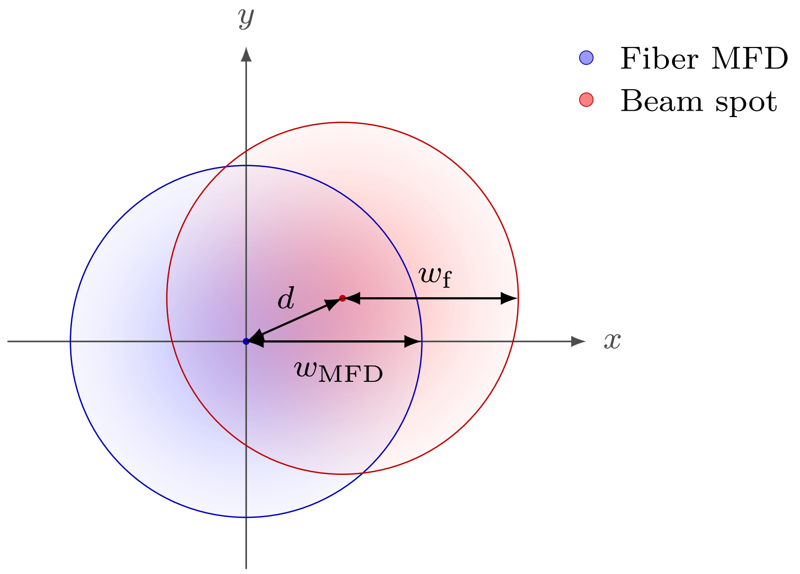

Figure 2.3: Cross-section schematic of the overlap between the fiber MFD (blue) with radius w_f and an incident Gaussian beam spot (red) with radius w. A lateral mismatch between the beam and fiber center is illustrated by the displacement d.

For multimode fibers, several guided modes can carry power at the same time [30]. Mode-matching to a single transverse field is therefore not required in the same way as for an

SMF. Instead, coupling can be treated mainly as a geometrical problem, where efficient coupling requires that the spot on the fiber endface fits within the core and that the tilt is within the acceptance cone set by the fiber NA. Misalignment such as lateral offset and angular tilt reduces η by decreasing the geometric overlap between what is launched and what the fiber can accept [29].

2.4.6 Stimulated Brillouin Scattering (SBS) and Other Fiber Nonlinearities

As in any dielectric material, sufficiently intense electromagnetic fields can give rise to nonlinear optical effects that affects propagation [31]. These nonlinear responses originate from the anharmonic motion of bound electrons driven by the electric field, which makes the induced polarization of the material nonlinear. The material response can therefore be described by expanding the polarization in powers of the electric field, where different nonlinear effects are associated with different orders of electric susceptibility.

The first-order susceptibility corresponds to the linear optical response and is included in the ordinary n and linear attenuation of the fiber [31]. The second-order susceptibility is generally negligible in fibers because of the molecular symmetry of silica glass. Therefore, the lowest-order nonlinear effects that are usually relevant for silica-fiber propagation originate from the third-order susceptibility. The dominant effects in this order are nonlinear refraction and stimulated inelastic scattering.

Nonlinear refraction corresponds to n having an intensity dependence known as the optical Kerr effect,

$$n = n_{\text{lin}} + n_2 I, \tag{2.31}$$

where n_{lin} is the linear refractive index and n_2 is the nonlinear refractive-index coefficient, a material-dependent parameter describing the strength of the Kerr effect [31]. For a single pulse, this can lead to self-phase modulation, where different parts of the pulse receive different nonlinear phase shifts because of the temporal intensity variation. This can broaden the optical spectrum, which enhances the effects of chromatic dispersion. Cross-phase modulation is a related effect where one optical field changes the phase of another field.

Stimulated inelastic scattering transfers energy from the incident optical field, called the pump wave, to a frequency-shifted scattered field through vibrational excitations of the fiber material [31]. The lower-frequency scattered field is called the Stokes wave, since part of the pump energy is transferred to the material excitation. The scattered wave can first be generated weakly through spontaneous scattering [32]. The stimulated process then occurs when the Stokes wave is amplified through further interaction with the pump wave, causing additional energy to be transferred from the pump to the Stokes wave.

The two main stimulated inelastic scattering processes in silica fibers are stimulated Raman scattering (SRS) and SBS [31]. SRS involves optical phonons, whereas SBS involves acoustic phonons. Here, phonons refer to quantized vibrational excitations of the material. Although both processes can transfer energy away from the pump, they differ in directionality and gain bandwidth. SRS can occur in both forward and backward directions and has a broad gain spectrum, whereas SBS occurs in the backward direction in single-mode fibers and has a much narrower gain spectrum. This backward direction is a result of the phase-matching condition for the Brillouin process, where energy and momentum must be conserved between the pump wave, Stokes wave, and acoustic phonon [32].

Both SRS and SBS have threshold-like behavior, meaning that significant transfer of energy from the pump to the Stokes wave occurs only when the pump power is sufficiently high [31]. However, the Brillouin gain coefficient g_B is around three orders of magnitude larger than the Raman gain coefficient. SBS therefore generally reaches significant gain at lower pump powers compared to SRS.

The SBS intensity threshold for a continuous-wave (CW) pump I_th can be written as

$$g_\mathrm{B} I_\mathrm{th} L = \Theta, \tag{2.32}$$

where Θ is the dimensionless threshold parameter for which SBS is considered significant [33]. For a pulsed pump wave, however, the threshold is divided into two regimes depending on whether τ is larger than the fiber round-trip time $2t_\mathrm{g}$ or not. For $\tau \leq 2t_\mathrm{g}$,

$$I_\mathrm{th} = \frac{2\Theta}{g_\mathrm{B} v_\mathrm{g} \tau} \left(\frac{T_\mathrm{B}\Theta}{\tau} + 1 \right), \tag{2.33}$$

where T_B is the acoustic phonon lifetime. If $\tau > 2t_\mathrm{g}$, I_th can only be solved numerically through the modified Bessel function $I_0(\cdot)$ [33],

$$\begin{split} I_0\left(\sqrt{2\gamma\Lambda\bar{\tau}}\right) e^{-\bar{\tau}} + e^{-\bar{\tau}} \int_0^{\Lambda} I_0\left(\sqrt{2\gamma(\Lambda - y)\bar{\tau}}\right) \left(\sqrt{1+\gamma} - 1\right) e^{(\sqrt{1+\gamma}-1)y}\, dy \\ + \int_0^{\bar{\tau}} I_0\left(\sqrt{2\gamma\Lambda s}\right) e^{-s}\, ds = e^{\Theta/2}, \end{split} \tag{2.34}$$

where

$$\gamma = 2 g_\mathrm{B} I_\mathrm{th} v_\mathrm{g} T_\mathrm{B}, \tag{2.35}$$

$$\Lambda = \frac{L}{2 v_\mathrm{g} T_\mathrm{B}}, \tag{2.36}$$

and

$$\bar{\tau} = \frac{\tau}{2T_\mathrm{B}} - 2\Lambda. \tag{2.37}$$

These expressions show that SBS is governed by the relation between the optical intensity in the fiber and the SBS intensity threshold. SBS can therefore be mitigated by lowering the optical intensity, or by increasing the threshold through reduced Brillouin gain or a shorter effective interaction length between the pulse and the fiber.

3

Method

This chapter outlines the methods used to fulfill the aim and objectives of this thesis. It is divided into three main sections, describing the initial intended test bench setup, the implemented final configuration based on limitations and other discoveries during the work, as well as the different measurements performed to reach the conclusion.

3.1 Initial Intended Optical Test Bench Configuration

The initial test bench configuration designed for ER tests is shown in Fig. 3.1, including the LRF source, an alignment system, a baseline attenuation module and energy meters, the free-space–fiber coupling stage, and the fiber link. The different components of the setup and their intended roles are presented in the following subsections.

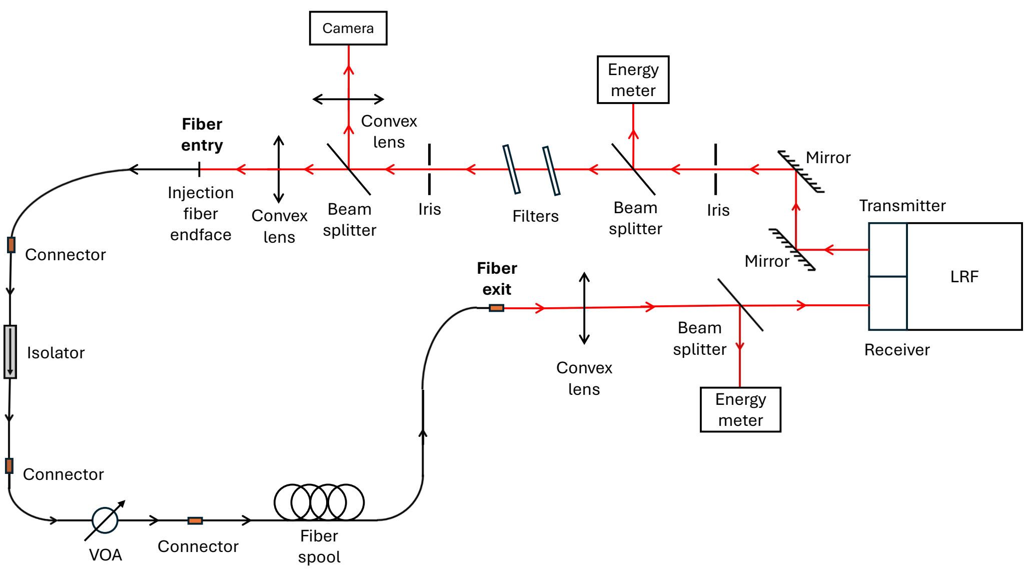

Figure 3.1: Optical schematic over the initially intended indoor test bench for performing LRF ER tests. The red path denotes free-space laser propagation, while the black path signifies fiber transmission. The arrows indicate the direction of travel.

3.1.1 Laser Rangefinder (LRF) Source

The laser source was the Heimdall LRF manufactured and developed by LPS. Heimdall is a pulsed laser with a spatially separate transmitter and receiver opening, where the receiver aperture diameter is $> 40\,\text{mm}$ [14]. The pulse specifications of the Heimdall LRF are presented in Tab. 3.1.

Table 3.1: Specifications of the Heimdall LRF from internal documentation [14], [34]. The pulse duration is defined as full width at half maximum (FWHM), and the beam diameter and divergence full angle at 90 % energy level. PRF stands for pulse repetition frequency. Missing value means not specified or not openly available.

Parameter	**Unit**	**Min.**	**Average**	**Max.**
Wavelength	nm	-	1535	-
Pulse duration	ns	-	15	-
PRF	Hz	Single pulse	1	2
Pulse energy	mJ	-	3.0	-
Beam diameter	mm	-	-	5
Beam divergence	mrad	0.8	1.0	1.2

3.1.2 Fiber link

The core part of the setup is the fiber link and the baseline design is displayed in Fig. 3.1, starting at “Fiber entry” and ending at “Fiber exit”. In the intended configuration, the fiber link consists of a short $\approx 1\,\text{m}$ single-mode patch cable (Thorlabs P3-SMF28Y-FC-2) connected to an in-line optical isolator (Thorlabs IO-H-1550APC). The isolator is a magneto-optic device that suppresses back-reflections, intended to prevent optical feedback into the free-space optics [35]. The isolator is then connected to a variable optical attenuator (VOA; OZ Optics DA-100-3A-1300/1550-9/125-S-60) meant as the fine-tuning device for the ER measurement. The VOA is, in turn, connected to the main 1.25 km SMF (Thorlabs SMF-28-J9). The total fiber guiding distance was intended to be in the same order of magnitude as in the OTA test configuration to keep the measurement conditions comparable.

The fiber components are interconnected using FC/APC connectors and corresponding mating sleeves (Thorlabs ADAFC3) [36]. The FC/APC connector endface is polished at an 8° angle to reduce back-reflections, while the mating sleeves allow direct physical contact between the connector endfaces. This results in a low insertion loss of $\approx 0.25\,\text{dB}$. For the fiber output, a fiber adapter plate (Thorlabs SM1FCA2) was included which partly compensates for the 8° angle of the FC/APC connector for easier coupling back into free-space.

3.1.3 Free-Space–Fiber Coupling Stage

The most delicate part of the setup is the free-space–to–fiber coupling stage, which determines how efficiently light is launched into the fiber and propagated through the system, see Sec. 2.4.5. The initial test bench coupling stage had the beam path divided into two almost identical arms using a beam splitter (Thorlabs BSW18), see Fig. 3.1. The two arms were intended to have the same length and two identical plano-convex lenses (Thorlabs LA1417-C). One arm would have focused the pulses onto the fiber facet, while the other arm would have focused the beam onto a 1550 nm sensitive laser beam profiler camera (Spiricon SP503U-1550). Because of the two identical arms, the camera would have displayed an image of the beam profile similar to the one entering the fiber. Consequently, a correlation between the beam position and the MFD of the fiber could be established. This is especially important since the pulse-to-pulse characteristics of the LRF, such as beam position, beam diameter, and pointing, are not completely identical, but can slightly deviate. These variations can be perfectly fine for intended distance measurements, assuming the LRF operates within its defined requirements, but might be problematic in the more sensitive free-space–to–fiber coupling. Pulses with characteristics that significantly reduce η could thus be disregarded during the ER measurement to make the results more representative of normal use. Once the reference position on the camera that corresponds to the fiber MFD had been established, it could also be used for alignment assistance if changes to the propagation prior to the coupling stage were to be made.

The fiber endface was planned to be held in place with a V-groove fiber clamp (Thorlabs HFF003), which in turn would be mounted on a three-dimensional linear transition stage (Newport M-462-XYZ-M) equipped with vernier micrometer manual actuators (Newport SM-25). The micrometers provide a direct readout in 10 µm increments, while the vernier scale permits interpolation with a nominal resolution of 1 µm [37]. The camera would be mounted on a single-axis translation stage (Thorlabs PT1/M) with a micrometer manual actuator (Thorlabs 150-801ME).

The LA1417-C plano-convex lens has the curvature radius $R_{\text{lens}} = 77.3\,\text{mm}$ and refractive index $n = 1.5008$ at $\lambda = 1535\,\text{nm}$ [22], which corresponds to $f = 0.154\,\text{m}$ using Eq. 2.20. With Eqs. 2.13–2.17 and the Heimdall pulse specifications in Tab. 3.1, the lens focusing waist $w_{\text{f}} \approx 28\,\mu\text{m}$ (assuming lens positioned 1 m from the LRF). This is $> 5w_{\text{MFD}}$, resulting in the coupling efficiency $\eta \approx 13\,\%$, assuming negligible tilt and lateral displacement, using Eq. 2.30.

In addition to lens availability, a larger w_{f} was considered a beneficial compromise. For pulsed operations with high peak power and low average power, the fiber is most susceptible to facet damage, which is a result of high peak power [38]. Using Eq. 2.5 as well as 2.6 with the Heimdall specifications in Tab. 3.1, $I_{\text{peak}} \approx 15\,\text{GW}\,\text{cm}^{-2}$ for $w_{\text{f}} = 28\,\mu\text{m}$. This is above the $\sim 1\,\text{GW}\,\text{cm}^{-2}$ practical safe limit given by Thorlabs [38], meaning added attenuation would likely be needed for safe propagation. Increasing the focused spot size rather than relying only on filters for increasing attenuation is beneficial in several ways. Firstly, it makes the coupling less sensitive to lateral misalignment, since small spatial deviations from the center of the MFD will have a lower effect on the transmitted energy. This is especially advantageous for pulse-to-pulse inconsistencies. It is also a more effective way to reduce intensity at the facet while retaining a better coupling efficiency as the spot size has a larger impact on the peak intensity compared to the coupling efficiency. This can be shown by introducing the radius ratio

$$q = \frac{w_{\text{f}}}{w_{\text{MFD}}} > 1, \quad \text{for } w_{\text{f}} > w_{\text{MFD}}. \tag{3.1}$$

Assuming $d = 0$, Eq. 2.30 becomes

$$\eta(q) = \left(\frac{2q}{q^2+1}\right)^2. \tag{3.2}$$

From Eq. 2.6, the relative peak facet intensity compared with a mode-matched focus is

$$\frac{I_{\text{peak}}(w_{\text{f}})}{I_{\text{peak}}(w_{\text{MFD}})} = \frac{1}{q^2}. \tag{3.3}$$

The coupling efficiency therefore decreases more slowly than the peak facet intensity, since

$$\frac{\eta(q)}{I_{\text{peak}}(w_{\text{f}})/I_{\text{peak}}(w_{\text{MFD}})} = \left(\frac{2q^2}{q^2+1}\right)^2 > 1, \quad \text{for } q > 1. \tag{3.4}$$

Thus, when $w_{\text{f}} > w_{\text{MFD}}$, the peak intensity I_{peak} at the facet is reduced more strongly than the coupling efficiency η. A larger w_{f} therefore provides a useful compromise between reducing the risk of high facet intensity, maintaining coupling efficiency, and improving resilience against lateral alignment variations.

Coupling back into free-space is not as sensitive as coupling into the fiber. Based on Eq. 2.19, the focal length required to collimate a beam with $w_{\text{f}} = w_{\text{MFD}}$ into the radius $W = 20\,\text{mm}$ corresponding to the minimum requirement of receiver aperture is $\approx 210\,\text{mm}$. A plano-convex lens (Thorlabs LA1979-C) with $f \approx 206\,\text{mm}$, calculated with Eq. 2.20 based on its $R = 103.0\,\text{mm}$ and $n = 1.5008$ at $\lambda = 1535\,\text{nm}$ [22], was planned. The fiber output adapter plate was intended to be attached to a mount (Newport U100-G ULTIMA) with manual actuators for adjusting angle in x and y direction to compensate for the slight angle remaining from the FC/APC connector and improve alignment with the LRF receiver aperture.

3.1.4 Baseline Attenuation Module and Pulse Energy Measurements

The initial setup included a planned filter stage to be able to adjust the needed baseline attenuation. It was to be positioned upstream the coupling stage and used in addition to the attenuation achieved from the mismatch between w_{f} and w_{MFD}, along with the loss from planned beam splitters to ensure fiber transmission without damaging components or introducing nonlinearities distorting the transmitted pulse, see Fig. 3.1.

In order to be able to track the fiber throughput, a beam splitter (Thorlabs BSW18) was planned to be connected to an energy meter positioned prior to the filter module as well as just upstream the LRF receiver, as shown in Fig. 3.1.

3.1.5 Beam Alignment System

In the baseline configuration, the main alignment system was intended to be positioned just downstream the LRF. It included two broadband dielectric mirrors (Thorlabs BB2-E04) capable of reflecting 99.95 % at 1535 nm [39] as well as two irises, see Fig. 3.1. The mirrors were to be mounted on kinematic mirror mounts (Thorlabs KM200) capable of fine angular adjustments in x and y. The purpose of this alignment system was to direct the beam through the optical components and optimize the free-space–fiber coupling by reducing the tilt. The first mirror was to be placed at an angle of approximately 45° from the incident beam, and the second mirror at around 45° from the reflected beam of the first mirror. The two irises were planned to be positioned in the optical path downstream the second mirror at the same height.

The alignment system would function by utilizing the first mirror to steer the reflected beam on the second mirror [40]. This would introduce a lateral shift on the beam downstream the two mirrors, which primarily adjusts the position of the beam on the first iris. The second mirror would then be used to angle the beam to mainly adjust for it to go through the second iris. The distance between the two steering mirrors affects how independently they control the beam, while the distance between the irises sets the sensitivity to pointing and thereby the accuracy of the alignment. To optimize the alignment for efficient coupling, the second iris was planned to be positioned as close to the beam splitter in the coupling stage as possible, depicted in Fig. 3.1.

3.2 Final Implemented Optical Test Bench Setup

The final test configuration is shown in Fig. 3.2, including the LRF source, an alignment system, a filter module and energy determination system, the air–fiber coupling stage, and the fiber link. The test bench was built on an optical table from Thorlabs with threaded holes separated by 2.5 cm in both horizontal directions. The deviations from the initially intended setup in Fig. 3.1 are presented and discussed below.

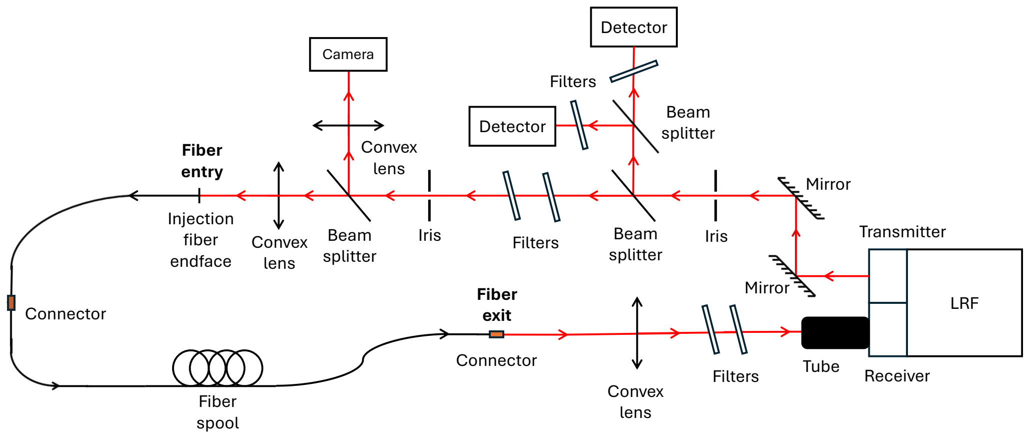

Figure 3.2: Optical schematic over the final implemented indoor test bench for performing LRF ER tests. The red path denotes free-space laser propagation, while the black path signifies fiber transmission. The arrows indicate the direction of travel.

Starting at the fiber-link, the final setup only consisted of the patch cable and the main fiber spool, as shown in Fig. 3.2. The isolator was never implemented because the key on its FC/APC connectorized endfaces was of a wider variant compared to the other components and the mating sleeves used, which meant it would not fit without significantly reducing coupling. It is still unclear why this was the case as Thorlabs only mention narrow-key as an alternative for connectorized isolators [35]. The isolator was, however, part of the components procured by T. Mingant [6] in 2025, which means there might have been a reason for this originally. The VOA was never implemented primarily because of uncertainty about the damage threshold for pulsed lasers as the only presented limit was for average power in combination with time constraints preventing further investigation. The attenuation needed to reach the ER was also significantly larger than the maximum capability of the VOA and the general uncertainty from other sources, like the free-space–fiber coupling , was likely larger than the steps in attenuation possible with adding separate filters. This way, the attenuation was added in the same way as it is for the OTA ER test, see Sec. 3.3.5.

It was realized during the measurements that the available energy meters were not sensitive enough to detect the pulses leaving the fiber. In addition, observing the pulse in the time domain was necessary to track distortions and nonlinear effects such as SBS. InGaAs detectors (Newport 818-BB-30) connected to an oscilloscope (PicoScope 5204) were therefore used instead. The detectors had a $50\,\Omega$ BNC output and were measured with matching $50\,\Omega$ termination at the oscilloscope input [41]. Additional optical filters were used to keep the detector signal below the saturation level. However, in the final setup to measure the ER, the second detector subsequent fiber transmission was never implemented, as seen in Fig. 3.2. This was due to time constraints in combination with the signal quickly becoming undetectable when additional attenuation was added. A baseline attenuation for which the pulse transmission through the fiber was stable had also already been established using the second detector, see Sec. 3.3.2.

The third main change was in the coupling stage. Another camera (Spiricon SP620U) with a bare silicon chip had to be used because the 1550 nm sensitive phosphor coating of the intended camera diffuses light, leading to a minimum measurable diameter of 600 µm [42], which is well above the estimated $2w_\mathrm{f} \approx 56\,\mu\mathrm{m}$. Even with the change of camera, the minimum accurately measurable diameter was limited by the pixel size to 88 µm. This meant that the originally planned identical arm, focusing half the beam onto the camera, had to be modified by using another plano-convex lens (Newport KPX124AR.18) with a significantly larger $f \approx 103\,\mathrm{cm}$, calculated from Eq. 2.20 using $R = 516.8\,\mathrm{mm}$ and $n = 1.5008$ at $\lambda = 1535\,\mathrm{nm}$ [43]. This resulted in a waist diameter of $\approx 367\,\mu\mathrm{m}$, which was above the minimum measurable value.

A separate trigger detector also had to be included because the camera required an external TTL trigger signal. This signal was generated using a wave generator, which was itself triggered by the optical pulse detected by the trigger detector. The detector used for pulse categorization could not be used for this purpose, since it had a specified saturation current of 5 mA [41]. With the $50\,\Omega$ termination used at the oscilloscope input, this corresponds to an estimated saturation voltage of approximately 250 mV, which is below the approximately 900 mV required to trigger the wave generator. The trigger signal was therefore obtained using an additional beam splitter (Thorlabs BSW18) positioned before the pulse-categorization detector, as shown in Fig. 3.2. The trigger detector was connected to the wave generator and protected with appropriate filtering.

Filters were introduced between the collimating lens and the LRF receiver to provide additional attenuation and protect the receiver from damage. This placement was chosen to increase the attenuation, while keeping the baseline attenuation and optical conditions prior to fiber coupling unchanged. However, reaching the ER required additional well-calibrated filters at $\lambda = 1535\,\text{nm}$. The only available filters were those normally used for the OTA ER measurement, which are mounted directly onto the transmitter. They therefore had to be placed before the coupling stage, changing the initial propagation conditions anyway, see Sec. 3.3.4. This meant that the camera could not be utilized in the final ER determination test.

3.3 Measurement Procedures

In this section, the different measurement procedures to build, align, and analyze the limitations of the test bench are described. The methods used to perform the final test bench ER measurement and the reference OTA ER measurement are also presented.

3.3.1 Optical Test Bench Construction and Alignment

The construction and alignment of the optical setup were carried out in three iterations. Initially, a simplified version of Fig. 3.2 was created where the coupling stage only consisted of the main arm that focuses the beam onto the fiber facet (beam splitters with second lens and camera as well as trigger detector not installed) and where the fiber-link only consisted of the $\approx 1\,\text{m}$ patch cable. The fiber output in this iteration was directly pointed at a second InGaAs detector to allow for temporal pulse profile comparison prior and subsequent fiber transmission. A filter mount was put between the fiber output and the detector where appropriate attenuation could be added to prevent saturation.

The ratio between the pulse peak after fiber propagation and the pulse peak prior to it was used as a relative measure of the fiber coupling. This peak ratio was not interpreted as an absolute coupling efficiency, since the initial reference detector captured a collimated beam, while the second detector measured part of the light cone leaving the fiber. However, it allowed relative changes in the fiber-transmitted signal to be compared between pulses and measurement configurations.

The first iteration was used to study the pulse transmission through the fiber in order to establish an appropriate baseline attenuation described in Sec. 3.3.2. The second iteration of the bench included the camera system, adding the beam splitter in the coupling stage to create the second arm with the $\approx 103\,\text{cm}$ focal length lens, as well as the trigger detector with corresponding parts described in Fig. 3.2. This configuration was used to perform the camera calibration portrayed in Sec. 3.3.3. The third and final test bench iteration corresponded to the configuration shown in Fig. 3.2 and was used for the final ER test presented in Sec. 3.3.4.

When constructing the optical test bench, the Heimdall was mounted into a fixture and screwed to a plate. The receiver of the LRF was aligned with the threaded holes in the table. This to simplify alignment of the optical path subsequent fiber propagation, since it lacks the mirror–iris alignment system present in the initial free-space propagation part. Because of the bulky mirror mounts and short distance between transmitter and receiver of the Heimdall LRF, the first mirror had to be positioned behind the fiber exit (from the perspective of the LRF) to not block the return signal. Except for this, the distances between all other optical components were kept to a minimum ($\approx 5\,\mathrm{cm}$) to limit the free-space propagation, which in turn minimizes alignment sensitivity as lateral displacements gets larger with increased distance for the same angle. The components were positioned at a height corresponding to the Heimdall transmitter, measured with a normal ruler. The fiber endface was initially approximately positioned at the lens focal length.

A first rough alignment of all optical components prior to, and including, fiber coupling was made with an alignment laser (Thorlabs PL201). The laser output was coarsely lined up with the LRF transmitter by mounting a tube on the transmitter side of the Heimdall fixture and using it as a reference for the laser mount. The tube was then removed, and the alignment laser turned on. The beam was adjusted to propagate through the free-space optics with the mirror–iris system described in Sec. 3.1.5 and the height of the components were adjusted for the beam to approximately hit them at the center. The fiber endface was adjusted in the xy-plane using the three-dimensional linear translation stage to be centered on the laser.

When the optical setup was properly configured for the alignment laser, the laser was removed and the LRF turned on. A baseline attenuation significantly above any potential damage region, based on the practical damage limit given by Thorlabs [38], was used to minimize risks. This attenuation was the highest level for which the pulses were still visible on a laser viewing card (Thorlabs VRC2). The mirrors were then adjusted slightly to center the beam through the irises by visualizing the pulses with the viewing card.

To optimize the fiber coupling, an initial transmitted signal was first obtained by adjusting the fiber position in the transverse xy-plane. A viewing card was used for the rough initial alignment, allowing the fiber end face to be positioned close to the focused beam. The focused intensity at the fiber input was also sufficient to produce small visible sparks on the V-groove fiber clamp holding the fiber. This helped with the more precise alignment, which allowed an initial signal response to be detected at the fiber output. No additional optical filters were used in front of the detector during this initial search, in order to maximize the detector response and make even weakly coupled pulses visible on the oscilloscope. Once a transmitted signal had been acquired, the fiber position could be optimized more efficiently by maximizing the pulse amplitude. Optical filters were then added when needed to keep the detector signal below the estimated $250\,\mathrm{mV}$ saturation limit.

After optimizing the transverse position, the axial position of the fiber was adjusted. As described in Sec. 2.4.5, efficient coupling requires the focused beam waist to be positioned at the coupling plane. Based on Eqs. 2.13–2.15 and 2.18, together with the Heimdall specifications in Tab. 3.1, the waist position was estimated as $z_\mathrm{f} \approx 3.7\,\mathrm{mm}$ behind the focal plane. The fiber was then translated along the optical axis using the axial actuator of the translation stage to find the position that maximized the transmitted signal. The recorded z_stage-values correspond to relative translation-stage readings, with $z_\mathrm{stage} = 0$ defined by the most forward position of the stage.

For each z_stage-position, the amplitude ratio between the subsequent fiber transmitted pulses and initial pulses was measured at the optimized transverse position. Each data point was obtained by averaging over 100 pulses. The axial position was first varied in relatively large steps away from the focal plane towards the waist. As long as the averaged pulse ratio improved, the scan was continued in the same direction. If the ratio decreased, the next position was chosen between the two best previous positions, biased toward the position with the larger ratio. This procedure was repeated until no significant improvement to the pulse ratio was observed.

When adding the camera system for the second iteration of the test bench, the beam splitter slightly translated the transmitted beam focused at the fiber. To optimize coupling again, the transverse alignment was repeated. The alignment of the camera to position it at the waist was performed visually until the beam profile appeared to be the smallest on the corresponding BeamGage software. It was then attached to the single-axis translation stage, adjusted in x and y to roughly center the beam on the chip. Since the focal length is large, the positioning is not as sensitive to small translations, but a final adjustment was made with the translation-stage manual micrometer actuator. The same procedure was repeated for the focal plane, but by looking at the divergence instead, see Sec. 3.3.3.

For the third and final iteration of the test bench used for the ER measurement, the free-space path subsequent the fiber was installed. The collimating lens was positioned roughly for the fiber output to be in the focal plane. The initial angle of the mount was initially adjusted for it to point in the general direction of the receiver. Two filters (Thorlabs NENIR240B), each with an attenuation of $\approx 37\,\mathrm{dB}$, were initially used to prevent damage to the receiver. A tube was also installed around the receiver to shield it from most reflections of the different optical components. The attenuation was then reduced until a range was detected. The angle of the fiber output mount was then adjusted as the ER measurement was performed, see Sec. 3.3.4.

3.3.2 Baseline Attenuation Determination

To ensure proper transmission without inducing damage or triggering nonlinear responses, a safe baseline attenuation was determined. This was carried out using the first bench iteration described in Sec. 3.3.1.

The test was performed by starting at a baseline attenuation well above the expected needed dampening based on the pulse parameters of the Heimdall in Tab. 3.1 required to stay above the practical damage threshold of $\sim 1\,\mathrm{GW\,cm^{-2}}$ established by Thorlabs [38].

The testing consisted of doing 100-pulse tests and recording the temporal pulse profile with the two detectors. The baseline attenuation was decreased by removing or changing filters between each pulse series until the intensity was large enough to start damaging the fiber or until a significant distortion of the pulse was induced by nonlinear effects. Damage was assessed based on a decrease in the peak ratio over a 100-pulse measurement, followed by a repeat measurement at an already tested stable attenuation level showing a clear reduction in coupling [44].

The steps in total attenuation were large initially, but reduced as the intensity closed in on the $1\,\mathrm{GW\,cm^{-2}}$ practical damage limit. The safe baseline attenuation level of the test bench was in the end chosen based on where disruption of the transmitted pulses started and with a significant safety margin.

3.3.3 Beam Profile Camera Calibration

As mentioned, the second iteration of the test bench described in Sec. 3.3.1 was used to perform the camera calibration measurements. Two different tests were made to study correlation between beam profile and coupling efficiency. They were both made with 300 pulses while recording the pulse prior and subsequent fiber at the same time with the two InGaAs detectors. The first test used the bare silicon chip SP620U camera positioned at the waist of the KPX124AR.18 lens. This was the main intended configuration. The software displayed the beam profile and recorded its centroid x and y coordinates as well as the e^{-2} diameter in x and y, among other stats. The additional attenuation used for the camera had to be very low due to the chip having very small absoption at $\lambda = 1535\,\text{nm}$. This made it quite noisy, even though it was calibrated for the background in the software. To reduce the noise impact, an aperture was utilized in the program to remove most of the background not containing the beam.

The second measurement used the initially intended phosphor coated SP503 camera, positioned in the focal plane. This was possible because the beam diameter in the focal plane was larger than the 600 µm minimum measurable diameter [42]. This camera was chosen because its phosphor coating provided higher sensitivity at the LRF wavelength, allowing additional attenuation to be used while still obtaining a detectable beam profile. The increased attenuation reduced the noise in the recorded profile.

Positioning the camera in the focal plane made it possible to determine the initial beam divergence, while lateral displacement of the centroid in this plane provided a measure of the incident beam pointing. The transmission ratio could therefore be evaluated as a function of both divergence and pointing. For each pulse, the centroid coordinates in x and y, the e^{-2} diameter in x and y, and the corresponding divergence in x and y were recorded.

3.3.4 Test Bench Extinction Ratio (ER) Determination

The ER measurement was made in conjunction with aligning the fiber output with the receiver. After an initial range detection was made, filters were screwed onto the transmitter side of the fixture holding the LRF until around 50 % of the pulses were detected. Then the angle on the fiber outlet mount was adjusted until all fired pulses were detected. This was repeated until no apparent improvement to the detection rate was made. The ER was then measured by recording the average detection rate for 100 pulses at different incremental attenuation levels until the 50 % detection rate mark was determined.

3.3.5 Over-the-Air (OTA) Extinction Ratio (ER) Reference Evaluation

The OTA reference test was performed based on an established LPS procedure [5] by using the same fixture utilized at the test bench. The fixture has a pre-calibrated scope attached, which was used to aim the transmitter onto the target. The fixture was positioned on top of a plate, which provided fine vertical and lateral adjustment. The LRF was aimed out of an opened window on the sixth floor of the LPS building at the target positioned at distance R_1. The time variable gain (TVG) function was turned off and the PRF set to 1 Hz before starting the ER test, as per instructions.

The specified extinction acceptance limit for the Heimdall LRF at LPS is ER $\geq 33.6\,$dB, defined as the point where the return signal detection is 50 % over 100 pulses with a false alarm rate of $< 1\,\%$. This at the distance $S_0 = 1000\,$m, the target reflectivity ρ_0 being 100 % Lambertian at $\lambda = 1535\,$nm, where the target is larger than the beam diameter, and at 100 % atmospheric transmission (no atmospheric attenuation) [14]. The conversion from the actual, well defined OTA test distance S_1, reflectivity ρ_1 at $\lambda = 1535\,$nm, and transmission $T_A^2 = 1$ (assumed 100 % transmission as mentioned in Sec. 1.1), is

$$\mathrm{ER} = \mathrm{ER}_{\mathrm{TEST}} - 10\log T_A^2 + 10\log\frac{\rho_0}{\rho_1} + 20\log\frac{S_1}{S_0}, \tag{3.5}$$

where $\mathrm{ER}_{\mathrm{TEST}}$ is the total attenuation added through filters to reach 50 % detection [5].

To determine $\mathrm{ER}_{\mathrm{TEST}}$, the reference ER test was performed during good visibility to reduce atmospheric attenuation. The total attenuation was initially set to a level well below the expected attenuation needed for 50 % detection and only 10 pulses were fired. This was repeated for incremental steps of added attenuation until the 50 % detection was reached. The measurement was then repeated for this level of attenuation with 100 pulses to verify that the defined 100-pulse average detection was close to 50 %. The finest available adjustment was approximately 1 dB, which meant that the test with 100 pulses was repeated with $\pm 1\,$dB to verify the total attenuation closest to 50 % detection. The determined $\mathrm{ER}_{\mathrm{TEST}}$ was then converted to the corresponding reference configuration ER with Eq. 3.5 and compared to the 33.6 dB threshold.

4

Results

This chapter presents the results gathered from experiments described in the Method chapter. It includes damage threshold determination, as well as both test bench and OTA ER tests.

4.1 Data Calibration

The FWHM pulse duration τ_{FWHM} was calculated from the data using the F1 method described by Rainio et al. [45]. The measured pulse is represented by sampled points (x_i, y_i), where $i = 1, 2, \ldots, n$, x_i is the time coordinate and y_i is the corresponding signal value. The F1 method determines τ_{FWHM} as the difference between the linearly interpolated right and left intersection points of the pulse with the horizontal half-maximum line

$$c_r = x_r - \frac{y_{\max}/2 - y_r}{y_{r-1} - y_r}\,(x_r - x_{r-1}) \tag{4.1}$$

and

$$c_l = x_l + \frac{y_{\max}/2 - y_l}{y_{l+1} - y_l}\,(x_{l+1} - x_l)\,. \tag{4.2}$$

The indices r and l denote the closest sampled points below $y_{\max}/2$, where $y_{\max}$ is the peak pulse value, on the right and left sides of the peak, respectively.

All data from the InGaAs detectors were corrected for specific attenuation put in their respective path to prevent saturation. The measured average pulse energy $E_{\mathrm{pulse}} \approx 2.35\,\mathrm{mJ}$, and all filters used to achieve needed attenuation were calibrated based on this energy and are compiled in Tab. A.1. The additional filters used specifically for the ER tests were pre-calibrated based on $\lambda = 1535\,\mathrm{nm}$.

Because of observed reduced coupling due to initial pulse instabilities when firing a series of pulses from the Heimdall LRF, the first 10 pulses were discarded for each test bench data set. All figures were generated using MATLAB R2022a.

4.2 Alignment

The coupling performance as a function of the translation-stage axial position z_{stage} is shown in Fig. 4.1. Five positions are displayed, each with 90 scattered peak amplitude ratios (initial 10 discarded) based on the two InGaAs detectors and a line between their respective average value. The distance measurement on the x-axis is the fine adjustment of the manual actuator in the axial direction of the translation stage. The reference position $z_{\text{stage}} = 0$ therefore corresponds to the foremost position of the translation stage, closest to the focusing lens, which was roughly positioned at the lens focal plane. As shown in Fig. 4.1, the greatest coupling performance was found at $z_{\text{stage}} = 1.0$ mm. Since the two measurement points 0.25 mm on either side of the maximum both decreased by approximately the same amount, this position was considered close to optimal coupling and was used for all subsequent measurements.

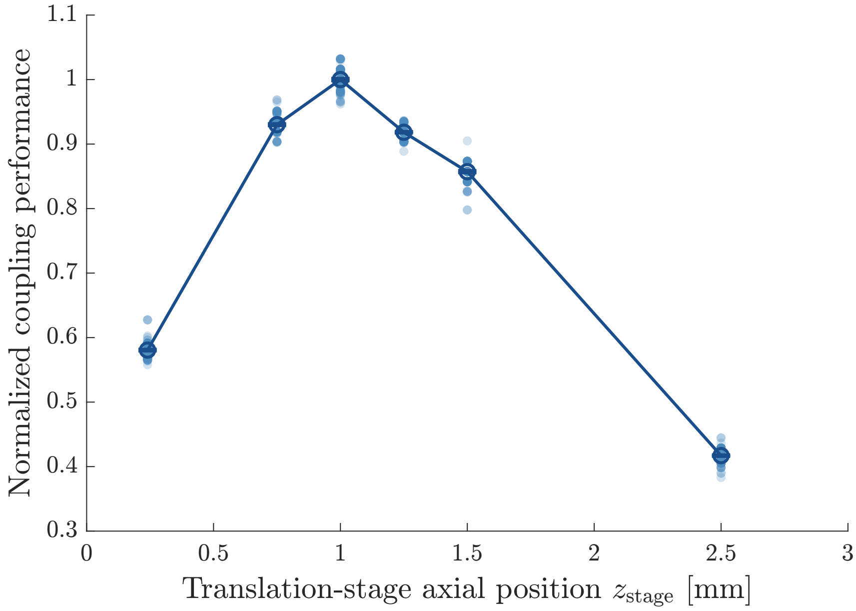

Figure 4.1: Normalized coupling performance as a function of the translation-stage axial position z_{stage}. The x-axis shows the fine adjustment of the manual actuator along the axial direction of the translation stage, with $z_{\text{stage}} = 0$ defined as the foremost stage position. Each measured axial position is represented by 90 peak amplitude ratios derived from the two InGaAs detectors. These are shown as partially transparent light-blue markers, so that regions with higher point density appear darker. The dark-blue circles represent the mean value at each position, connected by a dark-blue line to visualize the trend.

4.3 Baseline Attenuation Determination

The left panel of Fig. 4.2 presents how the pulse peak ratio between the two detectors develops over 90 pulses for different attenuation levels and the right panel a comparison of the 20.1 dB attenuation made initially compared with a repeat of the same attenuation level subsequent all the measurements in the left panel for the same fiber. None of the measurements shows a clear decrease in peak amplitude ratio as the pulse count increases, which suggests no apparent damage has been induced on the fiber. The ratio appears stable for the higher attenuated measurements, with increasing pulse-to-pulse differences as the attenuation decreases, which is partly expected since the oscillations become less dampened. The lower attenuated measurement series, especially the one with a total attenuation of 3.2 dB shows a more erratic pulse-to-pulse behavior though. This is a consequence of pulse distortion where the pulse tail was increasingly truncated as the attenuation decreased, see Fig. 4.4. For the measurement with an attenuation of 3.23 dB, the truncation extended past the pulse peak, which resulted in the pulse maximum being determined by the variations in truncation. It is, however, clear from the right panel of Fig. 4.2 that all peak ratios are lower for the retest compared to the initial measurement, which might suggest some permanent reduction in coupling. The mean reduction is ≈ 6%.

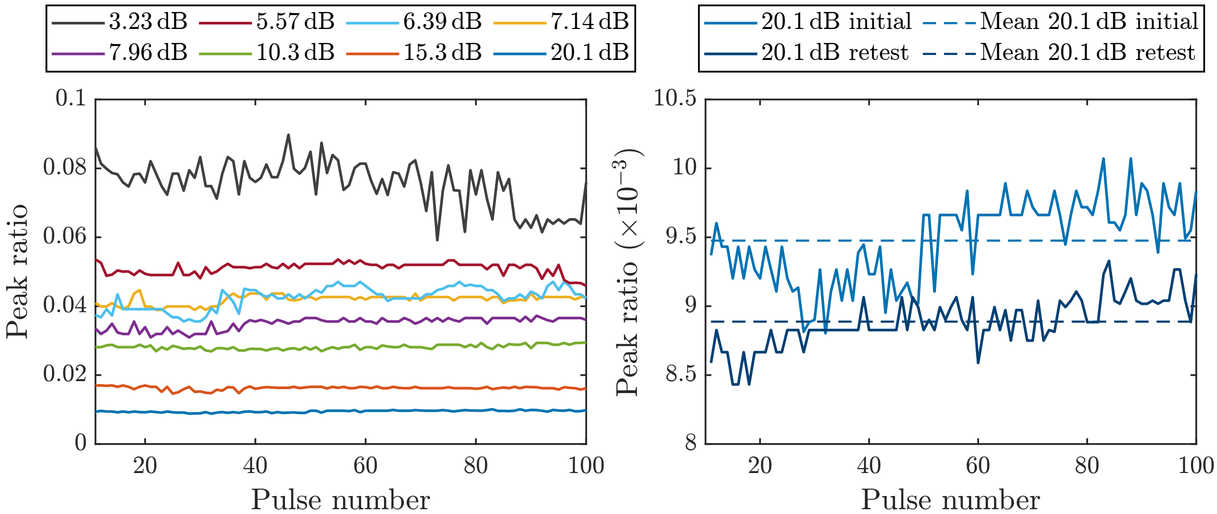

Figure 4.2: Peak pulse ratio between fiber transmitted pulse measured with InGaAs detector 2 and initial pulse measured with InGaAs detector 1 as a function of pulse number. First 10 pulses are discarded because of initial LRF pulse-to-pulse instabilities. Left plot shows peak pulse ratio evolution for different levels of attenuation and the right panel the difference between initial test with 20.1 dB attenuation compared to the same level of attenuation after going through all measurements displayed in the left panel.

Fig. 4.3 shows the evolution of the FWHM pulse duration τ_{FWHM} as the attenuation is decreased. The median τ_{FWHM} is consistently at ≈ 18.7 ns with a similar pulse-to-pulse difference until the attenuation reaches a threshold of ≈ 8 dB. At this point, the median decreases slightly and the pulse duration span increases. As the attenuation is decreased past this point, the reduction in τ_{FWHM} becomes drastic. The pulse-to-pulse span increases further, generally extending from high density around the median up to the original, undistorted duration. This shows a variety of the amount of truncation for a specific pulse strength, where the majority occur around the maximum. The trend shows a threshold attenuation level, under which the pulse response starts to become nonlinear. This is likely SBS described in Sec. 2.4.6, which depends on the intensity.

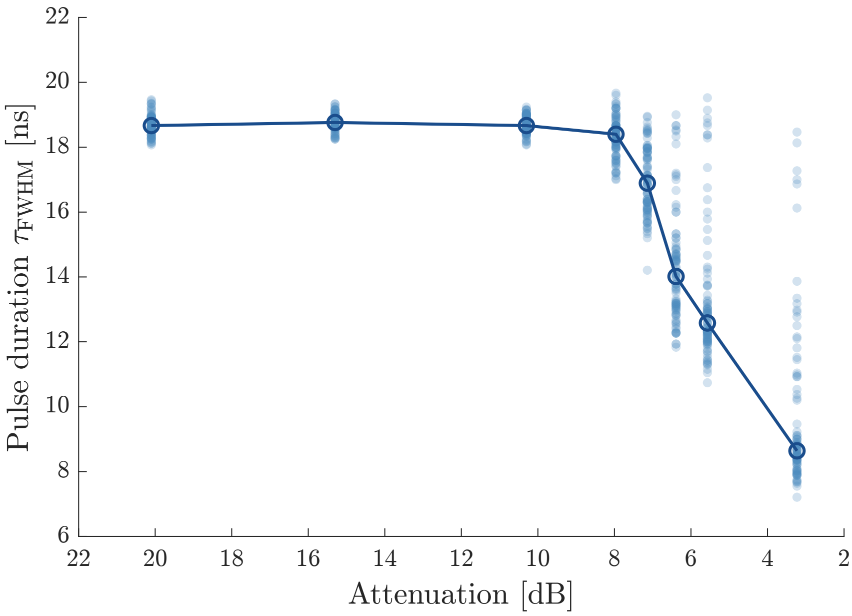

Figure 4.3: FWHM pulse duration for a decreasing amount of attenuation. Each half-transparent, blue scatter point represent the pulse duration of a single pulse in a 90 pulse measurement (the darker the blue, the higher the density) for a specific level of attenuation, with a darker blue circle representing the median pulse duration of the 90 pulse measurement. A line with the same dark blue color is drawn between the medians to visualize the trend.

The pulse-distortion for the four lowest measured attenuation levels, where the truncation is significant, is visualised in Fig. 4.4. Each panel shows, for a specific level of attenuation, a typical distorted pulse with an undistorted one from the same measurement for comparison, as well as a separately measured backscattered pulse. The forward propagating pulses are normalized from the same scale, while the backscattered pulse is normalized separately. The black vertical line represents the peak of the incident pulse for time comparison. The figure clearly displays how the distortion occurs at the tail of the pulse and how it happens earlier in the pulse with decreased attenuation, matching the decrease in τ_{FWHM} displayed in Fig. 4.3. It is also evident, although not as clear since the front propagating pulse does not have a completely flat tail, that the backscattered pulse shows an opposite shape to the distorted one with a drastic onset instead of a tail. This points to the tail of the pulse being backscattered as a consequence of SBS. The pulses also line up and correlate roughly in time, where the backscattered wave shifts with the truncation onset later in time as the attenuation is increased. This is consistent with the pulse tail being backscattered, likely as a consequence of SBS.

Some bias to the shape of the backscattered pulse is induced from an additional peak at around 10 ns that gets larger as the attenuation is increased, see Fig. 4.4. The peak occurs very close in time to the incident pulse, which likely means that this is an initial reflection from the optical components around the beam splitter, as the detector for backscattered light was positioned opposite the initial beam splitter by detector 1. The increase with attenuation points to this further as the filters were positioned downstream the detector, which likely means that this peak is roughly constant while the back scatter pulse is increasingly attenuated.

This also shows how the truncation occurs past the peak of the transmitted pulse when using 3.23 dB attenuation which means that each variation in the distortion affects the peak amplitude and therefore explains the erratic peak amplitude ratio behavior for this level of attenuation in Fig. 4.2. The other attenuation levels are more steady as the distortion is not strong enough to affect the peak amplitude.

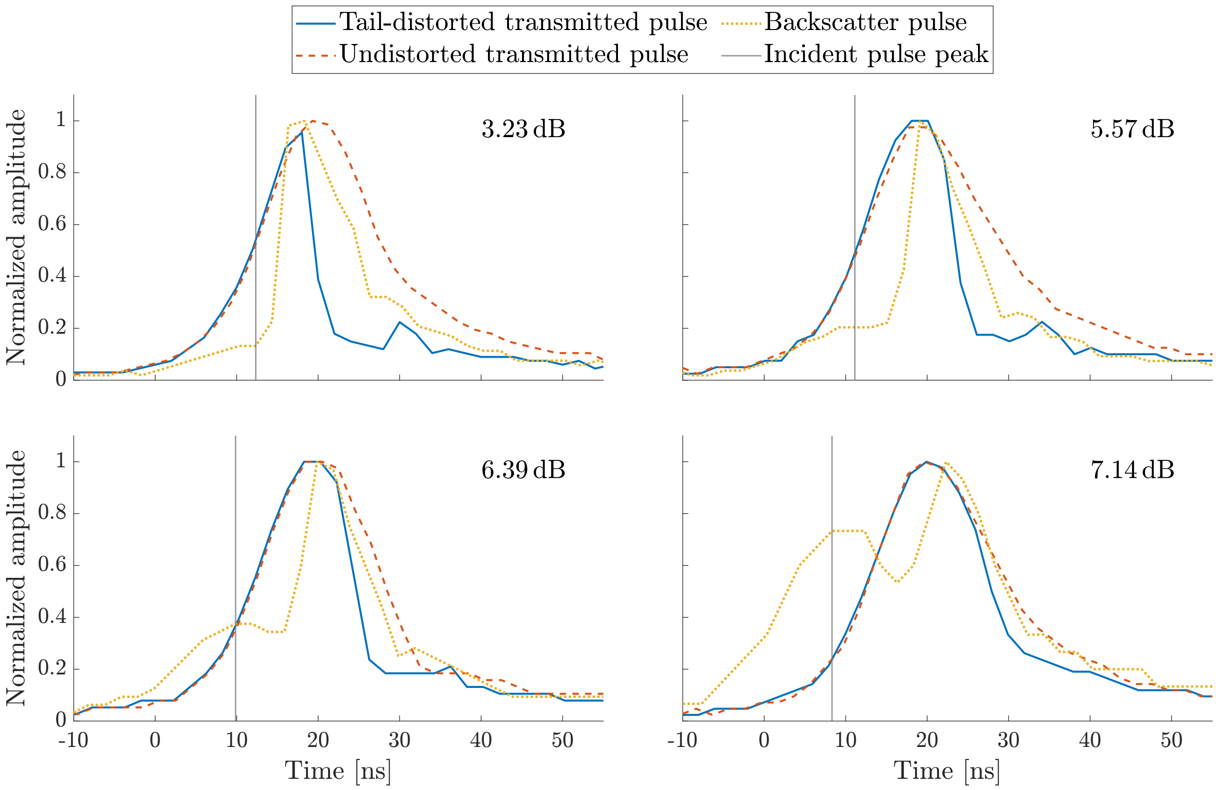

Figure 4.4: Visualization of decreased temporal pulse truncation (blue) with increased attenuation presented separately in each panel. An undistorted transmitted pulse (dashed orange) from the same measurement series is displayed in each panel for comparison as well as a separately measured backscattered pulse (yellow). A dark grey line is drawn in each window representing the incident pulse peak position in time.

Installing the final full fiber link changed the threshold and the distortion phenomena. The peak pulse ratio for different levels of attenuation for the full final fiber link is displayed in Fig. 4.5. Like for the short patch cable fiber measurements in Fig. 4.2, Fig. 4.5 shows how the peak ratio is stable for the two higher attenuated measurements but becomes erratic pulse-to-pulse at higher intensity, in this case for the 18.5 dB test and even more so when reducing it to 17.7 dB. However, this occurs for a significantly higher baseline attenuation when using the long fiber.

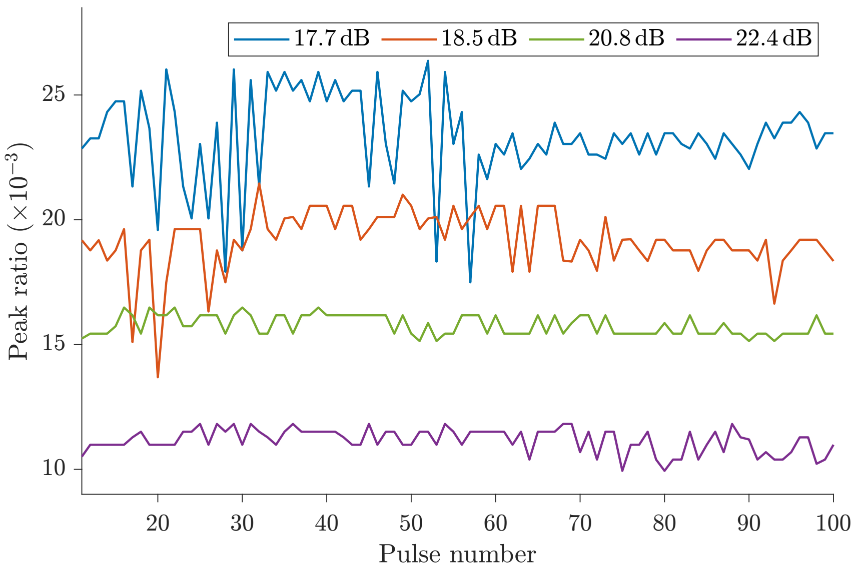

Figure 4.5: Peak pulse ratio between the two detectors as a function of pulse number for different levels of attenuation using the long fiber.

The effect on the temporal pulse shape was also different. Fig. 4.6 shows two normalized typical pulses from the 17.7 dB attenuated measurement, comparing the original temporal pulse shape from detector 1 with the transmitted pulse from detector 2. Instead of an increasing truncation of the pulse tail eventually affecting the pulse peak, the distortion affected the peak directly. Even though this partly explains why the pulse ratio would be affected at a higher attenuation, it is still significantly larger than the ≈ 8 dB level where the short fiber transmitted pulse started showing signs of tail truncation. Four additional pulses are displayed in Fig. A.1.

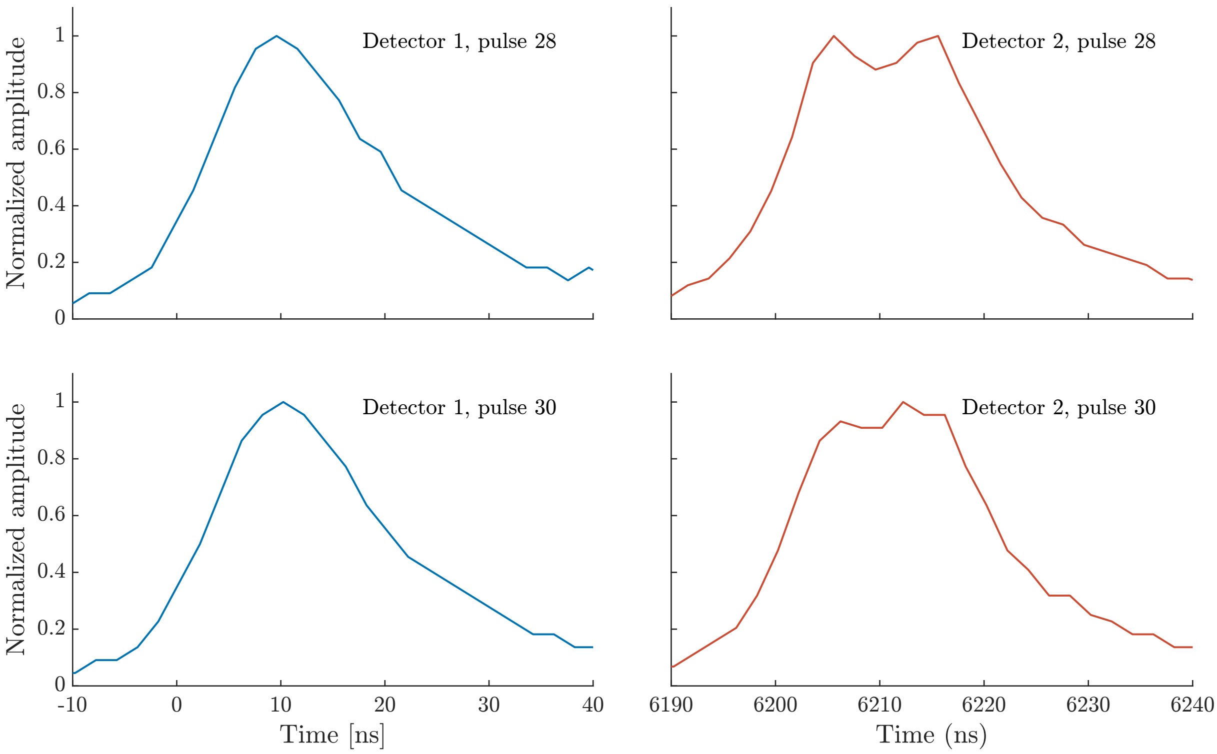

Figure 4.6: Comparison of temporal pulse shapes for two representative pulses from the 17.7 dB baseline attenuation measurement using the long fiber. The left panels show the incident detector pulses in blue before fiber propagation, while the right panels show the corresponding pulses after propagation through the fiber in red. The upper and lower rows correspond to the two selected pulses.

4.4 Beam Profiling Camera

Fig. 4.7 shows the pulse peak ratio in relation to the beam centroid position measured at the focused beam waist. The centroid was calculated in BeamGage, the software used with the camera, and is defined as the intensity-weighted mean position within a selected aperture. The left panel visualizes the centroid position for each pulse relative to the center of a circle corresponding to the fiber MFD in a 290 pulse measurement (initial 10 removed). The circle is scaled by the ratio of the focal lengths between the two different lenses in the coupling stage $1.03/0.154 \approx 6.69$, since f is the only parameter affecting the beam waist that changes when using the different lens as seen by Eq. 2.17. The center of the MFD circle, defined as the coordinate origin, was chosen as an effective best-coupling position, (x_c, y_c), estimated from the pulses with the highest peak ratio. This provides an experimental reference for the approximate center of the fiber mode field, since optimum coupling is expected when the beam is best aligned with the fiber mode, as described in Sec. 2.4.5. The plotted coordinates in the left panel are therefore defined as $\Delta x = x - x_c$ and $\Delta y = y - y_c$, while the MFD circle is shown only as a length-scale reference. The right panel instead shows the pulse peak ratio as a function of the radial distance from the center $r = \sqrt{\Delta x^2 + \Delta y}$ to visualize the points hidden below other points in the left panel. It is apparent from the figure that most pulses are bunched close together with some spreading in the positive y-direction, which suggests a generally stable pulse-to-pulse lateral variation for the LRF. No obvious correlation is observed between the centroid position and the peak ratio. This likely stems from the combination of having small lateral pulse-to-pulse variations for the LRF and the larger MFD–spot-size differential. There are, however, two distinct levels for the peak ratio, which suggests there being something affecting the coupling. The better coupled pulses are positioned close to the center of the MFD, but that is partly a result of how the center is defined.

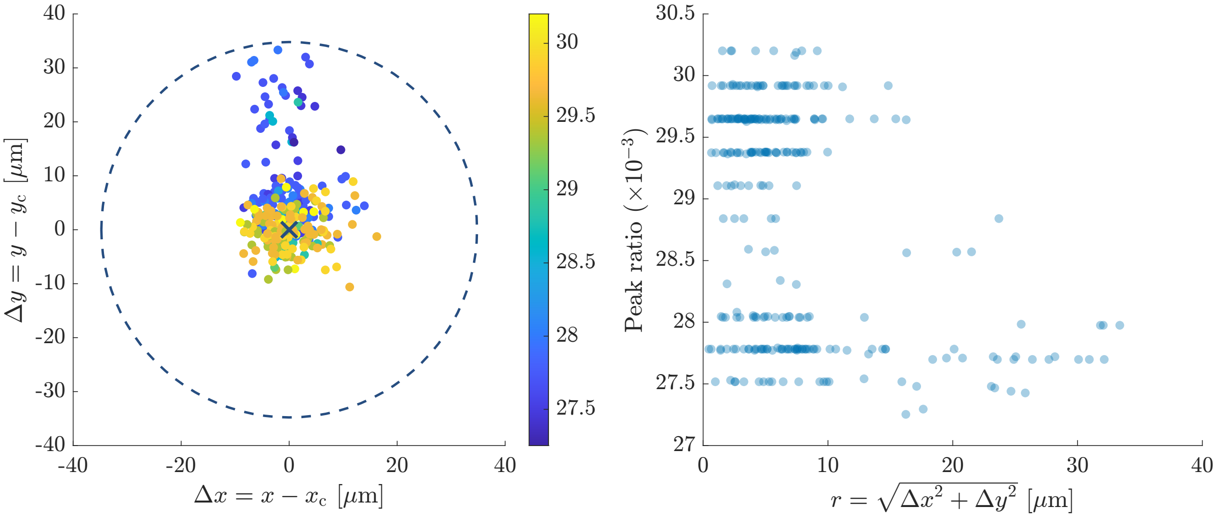

Figure 4.7: Pulse peak ratio between detector 2 and detector 1 as a function of beam centroid position measured at the focused beam waist. The left panel shows the centroid position of each pulse relative to the effective best-coupling position (x_c, y_c), with the plotted coordinates defined as $\Delta x = x - x_c$ and $\Delta y = y - y_c$. The colorbar represents the peak ratio and the dashed circle represents the fiber MFD scaled by the focal-length ratio between the camera and coupling lenses, used to visualize the fiber coupling plane. The right panel shows the same pulse peak ratio as a function of radial distance from the effective center, $r = \sqrt{\Delta x^2 + \Delta y^2}$, to make overlapping points easier to visualize.

Fig. 4.8 shows the pulse peak ratio, the normalized pulse peak signal for each detector separately, and the beam diameter, all as a function of pulse number. The peak ratio shows two clear regions of different coupling, as earlier mentioned. The middle panel shows that this change in peak ratio stems from both a reduction of the pulse peak for detector 1 and an increase for detector 2 at the same time. This suggests that the change in peak ratio is not only caused by a simple loss or gain in the total pulse signal, but rather by a redistribution between the reference detector path and the fiber-coupled detector path.

The lower panel shows an initial significant jump in beam diameter, followed by two general regions with different diameters. These two more stable diameter regions correspond approximately to the two regions in peak ratio, with the shift occurring around pulse 150. From a coupling-efficiency standpoint, however, a larger deviation from the MFD should result in lower efficiency for an ideal Gaussian profile, see Eq. 2.30. The opposite trend is apparent in the figure, and the initial spike in diameter does not produce a corresponding change in coupling. This suggests that the measured diameter change is not the direct cause of the coupling variation, likely because the diameter variation is small compared with the large focused spot size used in the experiment. The average measured waist radius $w_\mathrm{f} \approx 37\,\mu\mathrm{m}$.

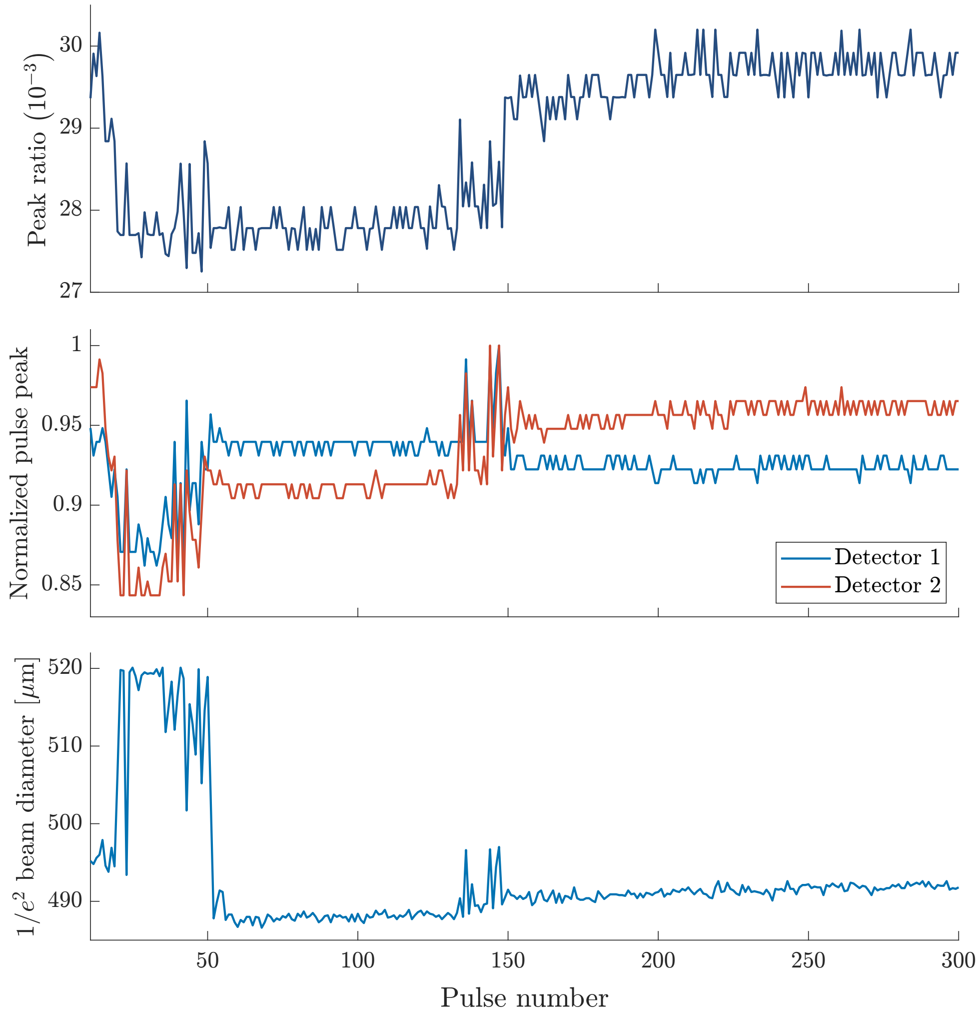

Figure 4.8: Pulse peak ratio, normalized detector peak signals, and measured e^{-2} beam diameter as a function of pulse number. The upper panel shows the coupling-related peak ratio (dark blue), while the middle panel shows each detector separate (detector 1 = blue, detector 2 = orange). The lower panel shows the measured beam waist diameter (blue).

Fig. 4.9 is similar to Fig 4.7, but here the coordinates represent relative pointing angles based on the phosphor coated camera positioned in the focal plane. The pointing angles were estimated from the focal-plane centroid displacement using $\alpha_x \approx (x_\mathrm{f} - \tilde{x}_\mathrm{f})/f$ and $\alpha_y \approx (y_\mathrm{f} - \tilde{y}_\mathrm{f})/f$, where f is the focal length of the diagnostic lens and $(\tilde{x}_\mathrm{f}, \tilde{y}_\mathrm{f})$ is the median focal-plane centroid position. The origin therefore represents the typical pointing direction during the measurement, rather than an estimated best-coupling position as in Fig. 4.7.

The left panel shows the pulse-to-pulse pointing coordinates α_x and α_y, where the color represents the peak ratio, while the right panel shows the peak ratio as a function of the pointing magnitude $|\alpha| = \sqrt{\alpha_x^2 + \alpha_y^2}$. The results indicate good pulse-to-pulse pointing stability for the Heimdall LRF and there seems to be no correlation between the pointing angle and the coupling in this µrad regime.

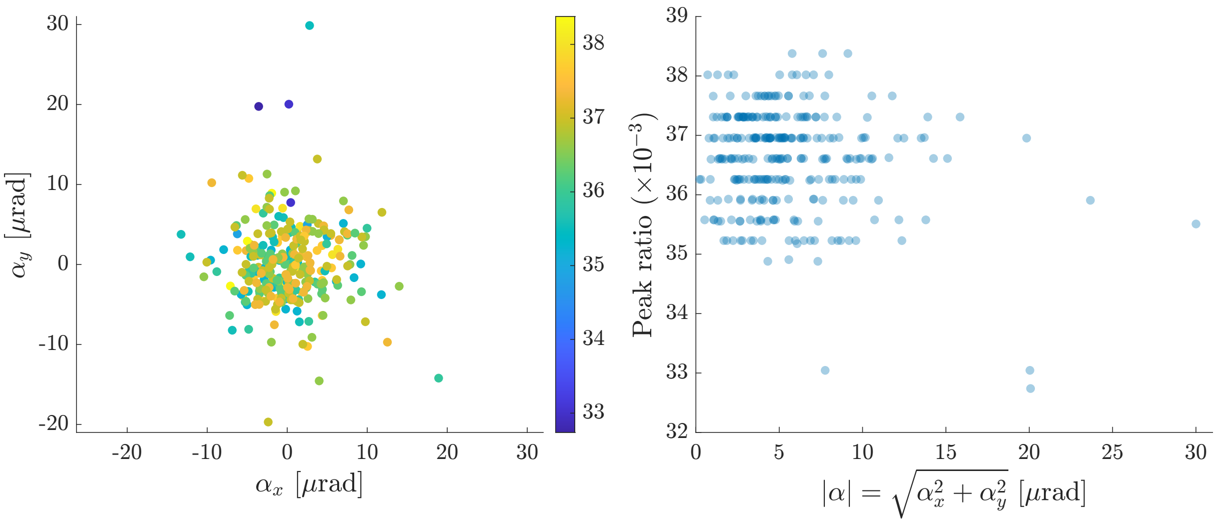

Figure 4.9: Pulse peak ratio as a function of pulse-to-pulse pointing variation measured using the phosphor-coated camera in the focal plane. The pointing angles were estimated from the focal-plane centroid displacement relative to the median centroid position, using $\alpha_x \approx (x_\mathrm{f} - \tilde{x}_\mathrm{f})/f$ and $\alpha_y \approx (y_\mathrm{f} - \tilde{y}_\mathrm{f})/f$. The left panel shows the relative pointing coordinates for each pulse, with color indicating the peak ratio. The right panel shows the peak ratio as a function of the pointing magnitude $|\alpha| = \sqrt{\alpha_x^2 + \alpha_y^2}$.

The half-angle divergences were effectively constant during the measurement, where $\theta_{\mathrm{div},x} \approx 0.37$ mrad, $\theta_{\mathrm{div},y} \approx 0.44$ mrad, and a combined $\theta_\mathrm{div} \approx 0.40$ mrad. The difference between the x- and y-components indicates a slightly asymmetric beam, but no significant pulse-to-pulse change in divergence was observed.

4.5 Over the Air (OTA) Extinction Ratio (ER) Test

The detection rate as a function of added attenuation from filters for the OTA ER reference test is shown in Fig. 4.10, with a dashed line corresponding to the 50 % detection threshold. The detection rate is constant at 100 % until the attenuation reaches ≈ 30 dB, after which the detection rate rapidly declines to 0 %. A detection rate of 48 % was reached over 100 pulses for an added filter attenuation of ≈ 32 dB. This was the closest achievable point to the 50 % ER detection threshold with the available filter stack and was therefore used as $\mathrm{ER}_\mathrm{TEST}$, which translates to the reference configuration ER ≈ 37 dB using Eq. 3.5. This is ≈ 3.4 dB higher than the acceptance threshold of 33.6 dB.

There was also a slight increase of ≈ 6 m on the average distance determined by the LRF when comparing the fully accurate distance achieved with no added attenuation and the distance at the ER.

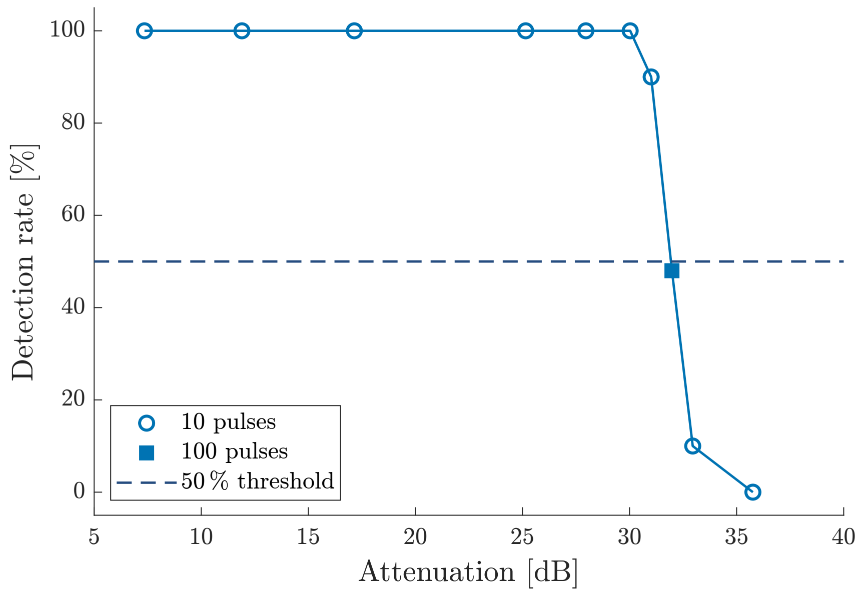

Figure 4.10: Eco pulse detection rate for different levels of added filter attenuation on the LPS OTA range for the Heimdall LRF. The specific measured data points are displayed with blue circles (10 pulses) or blue square (100 pulses). A blue solid line is drawn between the data points to visualize the trend and a darker blue dashed line representing the 50 % detection threshold for which the ER is defined.

4.6 Test Bench Extinction Ratio (ER) Test

The detection rate as a function of attenuation for the final test bench is displayed in Fig. 4.11, where the circles represent a 100 pulse average for that specific attenuation. The attenuation refers to the added attenuation from filters and beam splitters. Additional losses from coupling efficiency, fiber losses, alignment onto receiver aperture, and other sources are not included. The detection rate remained at 100 % until the attenuation reached $\approx$ 99 dB, after which it started to rapidly decline. In this region, the step-size in attenuation is $\approx$ 1 dB. The 50 % detection rate threshold for the ER point is represented by the dashed line. The measured detection rate closest to 50 % was 44 % achieved using an attenuation of $\approx$ 101 dB. For 100 dB and 102 dB the detection rate is 85 % and 0 % respectively. This attenuation is only the added dampening from filters and beam splitters.

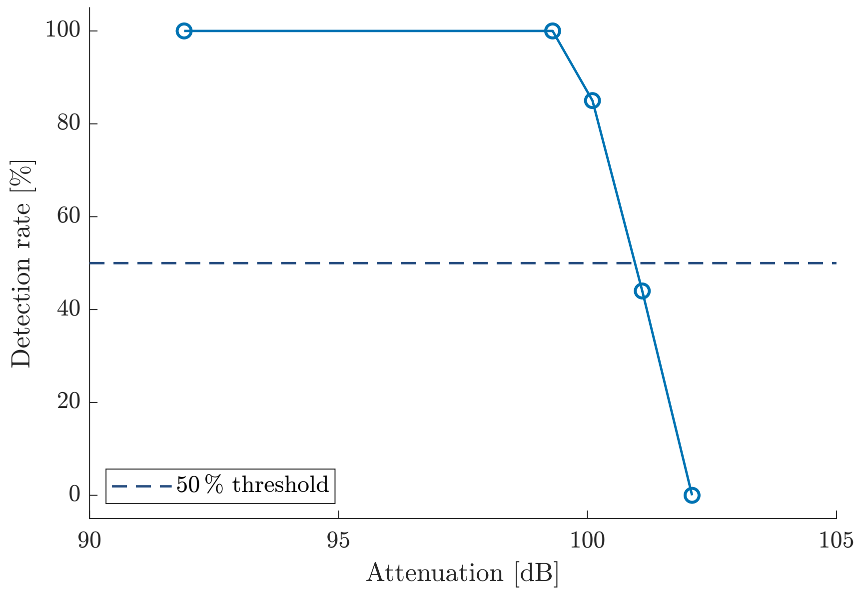

Figure 4.11: Detection rate as a function of added attenuation for the final indoor test bench. Each marker represents the average detection rate over 100 transmitted pulses at a given attenuation. The attenuation includes only the added damping from filters and beam splitters, while losses from fiber coupling, fiber propagation, receiver alignment, and other setup-dependent effects are not included. The dashed horizontal line marks the 50 % detection probability used to define the ER point.

Fig 4.12 shows how the determined average distance evolves with increasing attenuation towards the ER, both with TVG turned on and off. It shows the same trend as the OTA reference, where the measured range increases with the attenuation. Since the OTA test gave the correct distance for 32 dB below the ER, an equivalent attenuation reduction was used to determine the distance for the test bench. The distance determination with TVG turned on was performed because of initial reflections from the optical components being detected by the LRF for low enough attenuation with TVG turned off, disturbing the detection of the main pulse. As seen in the figure, the distance determination is not affected by TVG turned on, and the measured distance $\approx$ 28 dB below the ER was $\approx$ 925 m. Since the LRF reports one-way distance by halving the measured round-trip distance, as described in Sec. 2.1, the reported distance of $\approx$ 925 m corresponds to a total propagation distance of $2 \times 925 = 1850$ m. However, this is not the actual physical propagation distance in the test bench. It is the free-space distance that would give the same time of flight, since the LRF assumes propagation in free space while most of the propagation in the test bench occurs inside the fiber. The actual total distance is $\approx$ 1253 m with $\approx$ 1251 m fiber and $\approx$ 1.5 m free space. Based on the effective group index of the Corning SMF-28 ULL fiber $n_g = 1.4620$ [46], which should be close to the the group index of the Thorlabs SMF-28-J9 used in this case, the corresponding theoretical free-space distance is $\approx$ 1830 m using Eq. 2.27. The difference in 20 m between the actual free-space equivalent distance and the measured distance corresponds to $\approx$ 1 %, which could stem from the group index not being fully accurate.

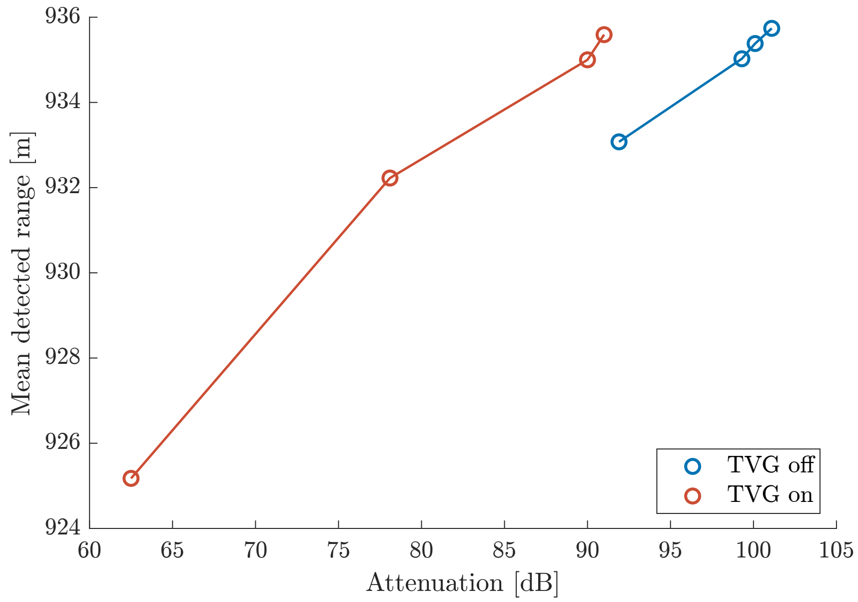

Figure 4.12: Average measured distance as a function of attenuation relative to the ER point for the final indoor test bench, shown with TVG turned on (red) and off (blue).

5

Discussion

This chapter includes a discussion about the results of the different measurements. The main discussion topics include the coupling and propagation element for the test bench configuration, the final ER test in comparison with the OTA test range, as well as measurement limitations and uncertainties in addition to potential improvements in the future.

5.1 Test Bench Configuration

To create a controlled laboratory complement to OTA ER testing without relying on weather conditions and atmospheric attenuation, the test bench must provide reliable and measurable pulse transmission through the fiber. This requires stable free-space-to-fiber coupling and controlled propagation, where proper axial alignment of the focused beam is a necessary first step. The results confirmed this importance, as Fig. 4.1 shows that the coupling is almost halved when the beam waist position is translated 1,mm from the fiber endface. This sensitivity is expected from the SMF mode-matching theory in Sec. 2.4.5, since axial displacement changes both the beam diameter and wavefront curvature at the fiber endface, reducing the spatial and phase overlap with the guided mode.

Fig. 4.2 displayed no apparent reduction in peak ratio pulse-to-pulse during the measurements for any the baseline attenuation levels. The repeated 20.1 dB measurement shows a slight reduction in the pulse ratio, but not significant enough to suggest obvious damage to the fiber. Paries et al. [44] reported irreversible reduction in amplitude of the throughput signal over time as the most indicative sign of damage. They also show how the fiber endface darkens under an optical microscope as the damage intensifies. Examining the fiber endface was not possible in this project as the instruments available did not provide sufficient resolution for the small fiber MFD of 10.4 µm. However, before reaching a large enough intensity to cause the potential onset of damage, unwanted nonlinear responses in the fiber, likely being SBS, started occurring, and evidently became the limiting factor guiding the needed baseline attenuation prior to fiber coupling.

Fig. 4.3 clearly displays the threshold-like phenomena indicative of SBS and Fig. 4.4 shows how the truncated part of the pulse is being backscattered, also consistent with SBS as described in Sec. 2.4.6. The nonlinear response started at around 8 dB, which corresponds to a maximum intensity of $\approx 2.4 \times 10^{12}\,\mathrm{W\,m^{-2}}$ using the measured $E_{\mathrm{pulse}} \approx 2.35\,\mathrm{mJ}$ with Eq. 2.5 and 2.7.

Since the pulse duration was longer than the round-trip time for the short $\approx 1\,\mathrm{m}$ fiber used in this measurement, the corresponding theoretical SBS threshold intensity was estimated numerically using Eq. 2.34. Cavillon et al. [47] report $g_{\mathrm{B}} = 2.4 \times 10^{-11}\,\mathrm{m\,W^{-1}}$ for conventional SMF-28 fibers, while Keaton et al. [33] established $\Theta \approx 22$ for high peak power pulses. The group velocity was approximated as $v_{\mathrm{g}} \approx 2.05 \times 10^{8}\,\mathrm{m\,s^{-1}}$, using Eq. 2.26 with the Corning SMF-28 ULL $n_{\mathrm{g}} = 1.462$ [46].

Motil et al. [48] discuss the Brillouin linewidth $\Delta\nu_{\mathrm{B}}$ for pulsed operation, which is related to the acoustic lifetime by

$$T_{\mathrm{B}} = \frac{1}{2\pi\Delta\nu_{\mathrm{B}}}. \tag{5.1}$$

They explain that for a standard SMF, the natural linewidth is approximately 30 MHz, but show that for pulsed operation, the effective Brillouin gain linewidth broadens when the pulse duration becomes shorter than approximately 50 ns, and approaches an inverse dependence on pulse duration for $\tau < 20\,\mathrm{ns}$. For a 15 ns pulse, Motil et al. specifically report $\Delta\nu_{\mathrm{B}} \approx 70\,\mathrm{MHz}$. Since the measured pulse duration of the LRF was $\tau_{\mathrm{FWHM}} \approx 19\,\mathrm{ns}$, $\Delta\nu_{\mathrm{B,eff}} = 70\,\mathrm{MHz}$ was used as an approximate effective Brillouin linewidth under low-nanosecond pulse conditions.

Using these values, I_{th} was determined numerically by first solving for γ using Eq. 2.34, with Λ and $\bar{\tau}$ evaluated from Eqs. 2.36 and 2.37. The resulting γ was then inserted into Eq. 2.35, giving $I_{\mathrm{th}} \approx 2.0 \times 10^{12}\,\mathrm{W\,m^{-2}}$. This corresponds to a baseline attenuation of $\approx 9\,\mathrm{dB}$. This is slightly lower than the measured threshold, especially since Keaton et al. define it at 20 % depletion. However, there are also additional losses from coupling that influences the actual coupled intensity. This means that the $\approx 8\,\mathrm{dB}$ baseline attenuation threshold in reality is quite a lot higher. Keaton et al. also assume a square pulse, while the LRF pulse is closer to Gaussian. Nevertheless, they describe SBS as a transient response affecting the pulse tail, which is consistent with the behavior observed in Fig. 4.4. The two threshold intensities being in the same order of magnitude in addition to the observed general propagation behavior strongly supports the nonlinear response being SBS.

As for the coupling, the results show no apparent dependence on geometrical properties of the pulse on the peak ratio, as presented in Sec. 4.4. As mentioned, this shows the benefit of using a focused beam waist significantly larger than the fiber MFD. Especially when a reduction of the intensity is required to prevent nonlinear effects during fiber transmission. However, something changed with the beam that made the initial pulse peak amplitude go down while the transmitted pulse peak amplitude increased, resulting in the step in peak ratio, see Fig. 4.8. This also caused a slight increase in the measured waist diameter visualized in the same figure.

A potential explanation to the increased coupling efficiency, not affected by waist diameter, lateral displacement, nor pointing, is a shift in the waist position. As demonstrated in Fig. 4.1, a slight shift of the waist from the coupling plane results in a significant reduction in coupling efficiency. A shift in the waist position would also explain the consequently larger waist diameter measured by the camera, since moving in either direction around the focused waist results in the beam diameter increasing. It could also be that the waist increases in addition to the waist shifting since the slight increase, in proportion to the mismatch between the waist and the fiber MFD, is negligible in terms of coupling. What causes this is unclear, but possibly a longitudinal mode shift of the transmitter of the LRF, perhaps causing a slight wavelength shift, which would affect the characteristics of the coating on the optical components. The proportion of light that is reflected from the beam splitters would change, which could explain the lower initial pulse peak amplitude of detector 1 as well as a larger proportion being transmitted to detector 2. It would also affect the focal length of the lens and therefore the waist diameter and its position.

After installing the fiber spool, the determined safe baseline attenuation based on the short fiber was no longer sufficient. As described in Sec. 4.3, a new threshold phenomenon appeared, occurring at a much lower intensity. The distortion affected the pulse peak instead of acting as a transient truncation of the pulse tail, suggesting it being an instantaneous response to the high intensity. It also appears to be a function of the length of the fiber, since it was not present for the 1 m fiber. However, it could still be SBS since the fiber transit time in this case is longer than the pulse duration, which means the intensity threshold for SBS is given by Eq. 2.33 instead. Inserting the same parameters as when calculating the theoretical threshold for the short fiber into the analytical equation, $I_{\mathrm{th}} \approx 1.7 \times 10^{12}\,\mathrm{W\,m^{-2}}$. This corresponded to an added attenuation of $\approx 10\,\mathrm{dB}$, which is way below the $\approx 19\,\mathrm{dB}$ where the pulse distortion first was measured in this case, see Fig. 4.5.

Ismagulov et al. [49] reported threshold-like amplitude reduction of spectrally narrow nanosecond pulses propagating through a SMF, which they attributed to modulation instability developing from noise. This was, however, for a 6 km long fiber, and the observed reduction was more uniform throughout the pulse rather than specific peak distortion.

Because of time constraints, the phenomenon could not be studied further. To establish the cause of the distortion, additional testing is required. However, the results were sufficient to establish a safe base attenuation level with proper pulse propagation to continue with ER tests.

5.2 Measuring Extinction Ratio (ER) on the Test Bench

A proper threshold roll-off region was established on the test bench as well as a measured range within $\approx 1\,\%$ of the theoretical equivalent, which is a clear indication on the configuration having the potential to be used as a way to determine the ER of LRFs.

The measured range increasing as the attenuation approaches the ER is a known phenomenon within LPS for the transmitter the Heimdall uses. Interestingly, this effect seems to be more significant for the test bench. For the OTA test, the reported range increased with about 6 m at the ER compared with no added attenuation, where it was fully accurate. A similar step in attenuation from the ER on the test bench resulted in a difference of almost twice that. This could also explain the range measurement being slightly above the approximate theoretical distance. The test bench might require further reduction in attenuation before showing the correct distance. This increased sensitivity could potentially prove beneficial when evaluating this phenomenon in the future.

The determined ER based on added attenuation to the setup corresponded to $\approx 101\,\mathrm{dB}$, as presented in Sec. 4.6. To compare this to the added $\approx 32\,\mathrm{dB}$ to reach the ER for the OTA test stretch, an estimate on each of the two specific setup configuration losses are required. For the Lambertian, extended target on the OTA configuration, The total transmission T_{OTA} corresponds to the lidar range equation [50]

$$T_{\mathrm{OTA}} = \frac{D_{\mathrm{r}}^2}{4R_1^2} T_{\mathrm{A}}^2 \eta_{\mathrm{sys}} \rho_1. \tag{5.2}$$

$D_{\mathrm{r}} \approx 40\,\mathrm{mm}$ is the receiver aperture and η_{sys} is the system transmission based of added filters and other optics, which in this case is the transmission corresponding to the added $\approx 32\,\mathrm{dB}$. This will be set to 1 when determining the attenuation specifically corresponding to the test configuration.

Inserting all parameters and converting to attenuation results in $\approx 100\,\mathrm{dB}$, assuming clean air $T_{\mathrm{A}}^2 \approx 0.8$ [51]. This means the total ER is around 130 dB.

Doing the same estimation for the test bench is a lot more difficult. The configuration specific attenuation comes from the coupling efficiency into the fiber, losses in the fiber link, aligning the fiber output on the receiver aperture, among other losses. The total fiber link loss is low, $\approx 0.5\,\mathrm{dB}$ based on the propagation loss $\leq 0.18\,\mathrm{dB\,km^{-1}}$ [52] and the attenuation from the mating sleeve $\approx 0.25\,\mathrm{dB}$ [36]. As for the coupling loss, an estimate can be made using Eq. 2.30 while assuming zero lateral offset. This results in an attenuation of $\approx 12\,\mathrm{dB}$ with $w_{\mathrm{MFD}} = 5.2\,\mathrm{\mu m}$ and measured $w_f \approx 37\,\mathrm{\mu m}$. This also assumes no tilt in the coupling plane, which is reasonable for small tilt angles since it roughly scales with the tilt angle squared [26], but becomes significant when reaching a few degrees. The beam itself was aligned well with low tilt using the two irises, but the fiber position in the V-groove fiber clamp, mounted on the translation stage, which in turn is mounted to the table, likely induced tilt which in reality would increase the attenuation.

The loss from aligning the fiber output with the receiver aperture is not quantifiable. Firstly, the distance to the collimating lens was slightly smaller than the focal length because of the translation stage used for alignment in x and y. Secondly, the tube around the receiver very slightly clipped one side of the aperture, which would have resulted in losses. Lastly, the x and y alignment was made with the help of the receiver by maximizing detection while increasing attenuation. This worked to some degree, but the fluctuations in detection pulse-to-pulse around the ER made it difficult to accurately optimize alignment without analyzing trends, which would require a significant time investment.

The total ER estimation for the test bench configuration therefore corresponds to $\approx$ 100 dB. Because of the many assumptions of perfect coupling and alignment, the test bench configuration attenuation estimate of $\approx 10\,\mathrm{dB}$ is largely underestimated. However, the fact that it is in the same order of magnitude as the OTA ER of $\approx 130\,\mathrm{dB}$, as well as the OTA ER being larger than the test bench ER, shows the potential of the test bench. In the end, if the ER is consistent when doing multiple measurements with removing and reinstalling the LRF into the setup, the bench can be calibrated to the well defined OTA test range. This might not be sufficient for final testing before delivering product to customer, but could potentially have use during development.

5.3 Measurement limitations and uncertainty

The measurements presented in this work should be interpreted as an initial evaluation of the test bench rather than a complete quantitative characterization. The aim is to investigate, develop, and evaluate the limitations of a test bench for carrying out ER measurements of LRFs in an indoor laboratory environment. Due to the complexity of the test bench and the many parameters affecting the propagation and detection of the laser pulses, a general measurement approach was required. Long repeated measurement series and detailed accuracy evaluations were therefore not feasible within the scope of this work.

Instead, the measurements were used to identify general trends, practical limitations, and the characteristics around the ER compared to the OTA test reference. The reported values should therefore mainly be interpreted as approximate estimates and relative comparisons rather than fully validated absolute quantities. As mentioned, important sources of uncertainty include alignment sensitivity, fiber coupling stability, pulse-to-pulse variations, detector sampling, and assumptions used in the theoretical estimates.

The main limitations of the instruments used came from the camera and the oscilloscope used to measure the temporal pulse profiles with the two detectors. The oscilloscope could only capture a measurement point every other nanosecond when using two separate detection points, which is a significant limitation for short nanosecond pulses. The phosphor coated camera available had the lower beam diameter limit 0.8 mm that it could capture accurately. Since this was not small enough to capture the waist, an equivalent camera without the coating had to be used, which only absorbed a fraction of the 1535 nm wavelength. This meant that the attenuation had to be significantly reduced and the dynamic range increased, which meant more background noise. The chip in the camera was also already partly damaged because of using low attenuation for similar measurements before, which likely also had an effect on the accuracy, even if a section of the chip that looked undamaged was used.

5.4 Potential Improvements to Investigate in the Future

A key addition to the test bench would be an energy meter that is sensitive enough to detect the highly attenuated pulses from the baseline that is used in conjunction with a fiber optic coupler. This way, a more exact measurement of the coupling efficiency can be determined and it can be connected directly to the fiber by separating part of the transmitted light like a beam splitter. In addition to this, a faster oscilloscope for better characterization of the pulses and a camera with appropriate coating that can capture smaller diameters accurately would improve the test bench.

Another improvement is to keep the propagation prior to the fiber coupling at the same baseline attenuation, as originally intended. This ensures constant operating conditions for calibration of the instruments and optical components. A VOA, as initially intended, could be used in the fiber link to allow for easier and finer adjustments of attenuation when determining the ER. Any additional attenuation needed on top of the VOA should be implemented downstream of the fiber, prior to the receiver. A more refined reflection shielding should also be implemented to prevent false detection as well as remove any clipping of the receiver aperture.

For ease of coupling, and better optimization, the fiber endface could be mounted on a motorized translation stage. This could be programmed as an alignment calibration that is used before performing ER tests on a new LRF device. Provided that an initial rough alignment is close to the waist and the center of the beam, the translation stage could scan in three dimensions while measuring the energy ratio or pulse peak ratio, and position the fiber where the optimal coupling occurs. This could, however, become challenging if the LRF transmitter changes mode during operation, since this may shift the waist position or change the optimal coupling point. This could likely be circumvented by setting a tolerance on the improvement during the scan.

There is also the aspect of aligning the fiber output on the receiver aperture. One potential fix for this would be to guide the output at a diffusive target plate and detect the echo signal, like for the OTA test but on smaller scale. A benefit of using a fiber when implementing this is that the fiber output essentially can be positioned wherever is required. This would also be beneficial for testing other LRFs than the Heimdall with different receiver configuration, since realignment would not be necessary. The downside is reflections around the room that could lead to false range detection, which would be difficult to eliminate.

Introducing an LRF with a different transmitter would affect the attenuation calibration, especially if the transmitter has larger pulse-to-pulse variations or a non-Gaussian beam profile. Since the test bench is currently optimized for the Heimdall, it would likely need to be adapted for different transmitter types. The camera in the coupling stage would be useful for this, as it allows the beam profile and coupling conditions to be monitored during both alignment and ER measurement, where non-detection because of pulse instabilities affecting coupling could be discarded.

Investigating the use of an MMF, especially the GRIN-MMF described in Sec. 2.4.4, could also be of interest. An MMF could improve coupling because of its larger core and because the incident field does not need to match a single Gaussian-like mode field as closely as in an SMF. This could be beneficial for non-Gaussian transmitter beams. However, the output field would be less well defined and would depend on which modes are excited, which could affect the spatial and temporal properties of the light reaching the receiver, even if the modal dispersion is reduced for the GRIN-MMF.

Future work should also include repeated ER measurements under identical conditions to quantify the repeatability of the setup and determine the statistical variation in the detection threshold region.

6
Conclusion

The aim of this thesis was to investigate, develop, and evaluate the limitations of an indoor laboratory test bench for carrying out ER measurements of LRFs. The purpose was to provide a possible complement to OTA ER testing, allowing LRF behavior to be verified during development and final performance testing independently of weather conditions. The test bench was based on coupling the transmitted LRF pulse into a single-mode fiber, guiding it through a controlled optical path, and adding attenuation until the ER region was reached. The setup was evaluated by characterizing the fiber coupling, determining a suitable baseline attenuation before fiber injection, and comparing the ER behavior with an OTA reference measurement.

The results showed that nonlinear propagation in the fiber was a central limitation of the test bench. For the short fiber, increasing the launch intensity caused truncation of the transmitted pulse tail together with a corresponding backscattered signal. This behavior was consistent with SBS, and the estimated SBS threshold was in the same order of magnitude as the experimentally observed onset. When the longer fiber spool was introduced, a different nonlinear pulse distortion appeared at lower intensity and affected the pulse peak directly. The exact mechanism could not be identified within this work, but the result showed that nonlinear fiber propagation must be controlled in order to obtain reliable pulse transmission through the test bench.

The beam profiler measurements showed that the coupling could be made less sensitive to ordinary pulse-to-pulse variations in beam position, beam diameter, and pointing by using a focused beam diameter significantly larger than the fiber MFD. This was beneficial for the test bench, since the launch intensity had to be reduced anyway to avoid nonlinear effects in the fiber. The remaining step-like coupling variation could not be explained by geometrical beam changes and was instead likely related to changes in the LRF transmitter behavior, potentially affecting the waist position or the response of the optical components.

The ER measurement on the test bench produced a clear threshold roll-off region, similar to the OTA reference measurement. A distinct ER point could therefore be identified, and the measured range agreed with the theoretically estimated equivalent distance within approximately 1 %. The test bench also showed a more pronounced increase in reported range when approaching the ER, indicating that it may be useful for studying this behavior under controlled conditions.

However, the test bench should still be regarded as an initial experimental implementation rather than a fully validated quantitative replacement for the OTA test range. The quantitative accuracy was limited by alignment sensitivity, coupling stability, pulse-to-pulse variations, detector sampling, camera limitations, attenuation calibration, and the incomplete characterization of setup losses. This was reflected in the estimated total attenuation at the ER, which was $\approx 110\,\text{dB}$ for the test bench compared with $\approx 130\,\text{dB}$ for the OTA reference. Since this test bench estimate relied on idealized assumptions regarding fiber coupling and receiver alignment, the total attenuation of the test bench should be interpreted as a lower-bound estimate.

Overall, the results show that the test bench has potential as an indoor complement to OTA ER testing. The main experimental principles were demonstrated, and the setup reproduced several relevant features of the OTA measurement, including the ER roll-off behavior and the range increase close to the detection threshold. However, further work is required before the test bench can be considered a reliable alternative for final performance testing prior to customer delivery. This should primarily include a more in-depth quantitative characterization of the setup, a more accurate determination of optical losses, and repeated ER measurements to evaluate repeatability.

Bibliography

[1] H. Ma, Y. Luo, Y. He, S. Pan, L. Ren, and J. Shang, "The short-range, high-accuracy compact pulsed laser ranging system," *Sensors*, vol. 22, no. 6, 2022, Art. no. 2146. DOI: `10.3390/s22062146`

[2] K. Chrzanowski, "Stations for testing laser range finders," in *Proceedings of OPTRO 2014 – International Symposium on Optronics in Defence and Security*, (OECD Conference Center, Jan. 28–30, 2014), Paris, France, 2014. Accessed: Feb. 18, 2026. [Online]. Available: `https://www.inframet.com/Literature/Stations_for_testing_laser_range_finders.pdf`

[3] Lumibird. "Lumibird is one of the world's leading specialists in lasers," Accessed: Feb. 18, 2026. [Online]. Available: `https://www.lumibird.com/en/the-group-about-lumibird/`

[4] Lumibird. "Military lasers rangefinders," Accessed: Feb. 18, 2026. [Online]. Available: `https://www.lumibird.com/en/military-lasers-rangefinders/`

[5] P. Ljungberg, "Acceptance test procedure," Lumibird, Paper 1791-UALM1170011/046, Nov. 2025, Unpublished.

[6] T. Mingant, "Investigation of telemetric bench extinction tester as a complement to over the air extinction measurement," Lumibird, Paper 1/0363-002/LXEL1080012, Aug. 2025, Unpublished.

[7] *LTF: Performance tester of laser range finders*, Inframet. Accessed: Mar. 19, 2026. [Online]. Available: `https://www.inframet.com/Data_sheets/LTF.pdf`

[8] *LUNI: Universal station for testing laser range finders/designators*, Inframet. Accessed: Mar. 19, 2026. [Online]. Available: `https://www.inframet.com/Data_sheets/LUNI.pdf`

[9] National Society of Professional Engineers. "Code of ethics," Accessed: Feb. 19, 2026. [Online]. Available: `https://www.nspe.org/career-growth/nspe-code-ethics-engineers`

[10] M. Hersh, "Professional ethics and social responsibility: Military work and peacebuilding," in *IFAC 2017 World Congress*, (Jul. 9–14, 2017), Toulouse, France, 2017, pp. 10 592–10 602. DOI: `10.1016/j.ifacol.2017.08.1316` Accessed: Feb. 19, 2026.

[11] "Militärstrategisk doktrin – MSD 22 [Military Strategic Doctrine – MSD 22]," Försvarsmakten, Doctrine, version 2.0, Jul. 1, 2022, In Swedish. Accessed: Feb. 19, 2026. [Online]. Available: `https://www.forsvarsmakten.se/siteassets/2-om-forsvarsmakten/dokument/doktriner/msd-22.pdf`

[12] "Strategic export controls in 2024 – military equipment and dual-use items," Government Offices of Sweden, Stockholm, Sweden, Government Communication Skr. 2024/25:114, 2025. Accessed: Feb. 19, 2026. [Online]. Available: `https://www.government.se/legal-documents/2025/07/skr.-202425114`

[13] H. N. Burns, C. G. Christodoulou, and G. D. Boreman, “System design of a pulsed laser rangefinder,” *Optical Engineering*, vol. 30, no. 3, pp. 323–329, Mar. 1991. DOI: 10.1117/12.55801
[14] S. Wickström and T. Uhrwing, “Requirement specification for LRF Heimdall,” Lumibird, Paper 1029-UALM1170001, Oct. 2010, Unpublished.
[15] F. Chiquet et al., “Improvement of the extinction ratio performance of a fiber laser based rangefinder by using successive real-time statistical algorithms,” in *Fiber Optic Sensors and Applications XIV*, ser. SPIE 10208, Anaheim, CA, US, 2017, 1020805. DOI: 10.1117/12.2262405
[16] ITU-T, “The use of the decibel and of relative levels in speechband telecommunications,” International Telecommunication Union, Recommendation ITU-T G.100.1, Jun. 2015. Accessed: Mar. 10, 2026. [Online]. Available: https://www.itu.int/rec/T-REC-G.100.1-201506-I/en
[17] R. Paschotta, *Gaussian pulses*, RP Photonics Encyclopedia, 2006. DOI: 10.61835/12e
[18] T. S. Khwaja and S. A. Reza, “Low-cost gaussian beam profiling with circular irises and apertures,” *Applied Optics*, vol. 58, no. 4, pp. 1048–1056, 2019. DOI: 10.1364/AO.58.001048
[19] B. E. A. Saleh and M. C. Teich, “Beam optics,” in *Fundamentals of Photonics, Part 1: Optics*, 3rd ed. Hoboken, NJ, USA: John Wiley & Sons, Inc., 2019, ch. 3, pp. 79–109.
[20] V. Myasnikov, “Efficient light coupling and propagation in fiber optic systems: Corrigendum,” *tbusphys*, vol. 2, no. 3, p. 0017, Sep. 2024. DOI: 10.54355/tbusphys/2.3.2024.0017
[21] R. Paschotta, *Focal length*, RP Photonics Encyclopedia, 2007. DOI: 10.61835/ldf
[22] Thorlabs. “N-BK7 plano-convex lenses (AR coating: 1050 - 1700 nm),” Accessed: Apr. 30, 2026. [Online]. Available: https://www.thorlabs.com/n-bk7-plano-convex-lenses-ar-coating-1050---1700-nm?pn=LA1417-C&aID=ae362d5a334552ed8bf5a1b79a8e5e84&aC=1&tabName=Tutorial
[23] R. Paschotta, *Chromatic aberrations*, RP Photonics Encyclopedia. DOI: 10.61835/1u3
[24] B. E. A. Saleh and M. C. Teich, “Fiber optics,” in *Fundamentals of Photonics, Part 1: Optics*, 3rd ed. Hoboken, NJ, USA: John Wiley & Sons, Inc., 2019, ch. 10, pp. 391–432.
[25] B. E. A. Saleh and M. C. Teich, “Electromagnetic optics,” in *Fundamentals of Photonics, Part 1: Optics*, 3rd ed. Hoboken, NJ, USA: John Wiley & Sons, Inc., 2019, ch. 5, pp. 160–208.
[26] D. Marcuse, “Loss analysis of single-mode fiber splices,” *Bell System Technical Journal*, vol. 56, no. 5, pp. 703–718, 1977. DOI: 10.1002/j.1538-7305.1977.tb00534.x
[27] R. Paschotta, *Mode radius*, RP Photonics Encyclopedia, 2007. DOI: 10.61835/o34
[28] Y. Bian et al., “Free-space to single-mode fiber coupling efficiency with optical system aberration and fiber positioning error under atmospheric turbulence,” *Journal of Optics*, vol. 24, no. 2, p. 025 703, 2022. DOI: 10.1088/2040-8986/ac3f8f
[29] W. Kam, Y. S. Ong, S. O’Keeffe, W. S. Mohammed, and E. Lewis, “An analytical model for describing the power coupling ratio between multimode fibers with transverse displacement and angular misalignment in an optical fiber bend sensor,” *Sensors*, vol. 19, no. 22, p. 4968, 2019. DOI: 10.3390/s19224968

[30] X. Liu, J. Guo, G. Li, N. Chen, and K. Shi, “Effect of lateral error on the coupling efficiency and beam quality of gaussian beam launched into large-core fiber,” *Optik*, vol. 187, pp. 185–192, Jun. 2019. DOI: 10.1016/j.ijleo.2018.11.172

[31] G. Agrawal, “Introduction,” in *Nonlinear Fiber Optics*, 5th ed. Waltham, MA, USA: Academic Press, 2013, ch. 1, pp. 1–25. DOI: 10.1016/C2011-0-00045-5

[32] G. Agrawal, “Stimulated brillouin scattering,” in *Nonlinear Fiber Optics*, 5th ed. Waltham, MA, USA: Academic Press, 2013, ch. 9, pp. 353–396. DOI: 10.1016/C2011-0-00045-5

[33] G. L. Keaton, M. J. Leonardo, M. W. Byer, and D. J. Richard, “Stimulated brillouin scattering of pulses in optical fibers,” *Optics Express*, vol. 22, no. 11, pp. 13 351–13 365, 2014. DOI: 10.1364/OE.22.013351 [Online]. Available: https://doi.org/10.1364/OE.22.013351

[34] S. Wickström, “General item specification for LRF Heimdall,” Lumibird, Paper 2243-UALM1170001, Mar. 2011, Unpublished.

[35] Thorlabs. “Ir fiber optic isolators with sm fiber (1290–2010 nm),” Accessed: Mar. 12, 2026. [Online]. Available: https://www.thorlabs.com/ir-fiber-optic-isolators-with-sm-fiber-1290---2010-nm?pn=IO-H-1550APC&tabName=Isolator%20Tutorial

[36] Thorlabs. “FC/APC fiber connectors: Single mode,” Accessed: Mar. 12, 2026. [Online]. Available: https://www.thorlabs.com/fcapc-fiber-connectors-single-mode?tabName=Overview

[37] Newport, *Vernier micrometer, 25 mm travel, 23 lb. load capacity, 50.8 TPI.* Accessed: Mar. 27, 2026. [Online]. Available: https://www.newport.com/p/SM-25

[38] Thorlabs. “Single mode fiber,” Accessed: Feb. 18, 2026. [Online]. Available: https://www.thorlabs.co.jp/single-mode-fiber?tabName=Damage%2520Threshold

[39] Thorlabs. “Fused silica broadband dielectric mirrors,” Accessed: Feb. 18, 2026. [Online]. Available: https://www.thorlabs.co.jp/fused-silica-broadband-dielectric-mirrors?tabName=Overview

[40] Thorlabs. “Two steering mirrors can be used to walk a laser beam to a new path,” Accessed: Feb. 18, 2026. [Online]. Available: https://www.thorlabs.com/two-steering-mirrors-can-be-used-to-walk-a-laser-beam-to-a-new-path

[41] Newport, *High speed photodetector, 800-1750 nm battery biased InGaAs detector, 2 GHz*. Accessed: Mar. 25, 2026. [Online]. Available: https://www.newport.com/p/818-BB-30

[42] OphirBlog. “A quick guide to profiling small laser beams,” Accessed: May 8, 2026. [Online]. Available: https://www.ophiropt.com/blog/a-quick-guide-to-profiling-small-laser-beams/

[43] Newport. “Plano-convex lens, N-BK7, 25.4 mm diameter, 1000 mm EFL, 1000-1550 nm,” Accessed: May 8, 2026. [Online]. Available: https://www.newport.com/p/KPX124AR.18

[44] F. Paries et al., “Optical damage thresholds of single-mode fiber-tip spintronic terahertz emitters,” *Optics Express*, vol. 32, no. 14, pp. 24 826–24 838, 2024. DOI: 10.1364/OE.525747

[45] O. Rainio, J. Hällilä, J. Teuho, and R. Klén, “Methods for estimating full width at half maximum,” *Signal, Image and Video Processing*, vol. 19, no. 289, Feb. 2025. DOI: 10.1007/s11760-025-03820-6

[46] *Corning SMF-28 ULL optical fiber portfolio*, Corning Incorporated, Corning, NY, USA, Feb. 2025. Accessed: May 15, 2026. [Online]. Available: https://www.corning.com/media/worldwide/coc/documents/Fiber/SMF-28%20ULL.pdf

[47] M. Cavillon, C. Kucera, T. W. Hawkins, N. Yu, P. D. Dragic, and J. Ballato, "Ytterbium-doped multicomponent fluorosilicate optical fibers with intrinsically low optical nonlinearities," *Opt. Mater. Express*, vol. 8, no. 4, pp. 744–760, 2018. DOI: 10.1364/OME.8.000744

[48] A. Motil, R. Hadar, I. Sovran, and M. Tur, "Gain dependence of the linewidth of brillouin amplification in optical fibers," *Opt. Express*, vol. 22, no. 22, pp. 27 535–27 541, 2014. DOI: 10.1364/OE.22.027535

[49] A. E. Ismagulov, S. A. Babin, E. V. Podivilov, M. P. Fedoruk, I. S. Shelemba, and O. V. Shtyrina, "Modulation instability of narrow-band nanosecond pulses propagating in anomalous-dispersion fibre," *Quantum Electronics*, vol. 39, no. 8, pp. 765–769, 2009. DOI: 10.1070/QE2009v039n08ABEH014011

[50] A. G. Kashani, M. J. Olsen, C. E. Parrish, and N. Wilson, "A review of LIDAR radiometric processing: From ad hoc intensity correction to rigorous radiometric calibration," *Sensors*, vol. 15, no. 11, pp. 28 099–28 128, 2015. DOI: 10.3390/s151128099

[51] I. I. Kim, B. McArthur, and E. J. Korevaar, "Comparison of laser beam propagation at 785 nm and 1550 nm in fog and haze for optical wireless communications," in *Optical Wireless Communications III*, (Nov. 5–8, 2000), ser. Proceedings of SPIE, vol. 4214, Boston, MA, United States, 2001, pp. 26–37. DOI: 10.1117/12.417512

[52] *Single mode fiber with ø900 µm hytrel jacket (SMF-28-J9)*, TTNO15884-S01, version Rev I, Spec sheet, Thorlabs, Feb. 6, 2024. Accessed: Feb. 18, 2026. [Online]. Available: https://www.thorlabs.com/item/SMF-28-J9

[53] Thorlabs. "Unmounted NIR absorptive ND filters," Accessed: Apr. 9, 2026. [Online]. Available: https://www.thorlabs.com/unmounted-nir-absorptive-nd-filters

A

Supplementary Measurement Data

This appendix contains supplementary measurement data used to support the results presented in Chap. 4. The data include component attenuation calibration values and additional pulse-shape comparisons from the long-fiber measurements.

A.1 Component Attenuation Calibration

Tab. A.1 shows calibrated attenuation levels from beam splitters and filters used to achieve the different attenuation levels presented in Chap. 4. The attenuation is calculated based of the measured average energy 2.35 mJ of the Heimdall LRF.

Table A.1: Average measured pulse energy after propagation through different components and corresponding attenuation relative to the Heimdall reference measurement.

Component	Average energy [mJ]	Attenuation [dB]
1st BSW18 Refl.	0.929	4.03
1st BSW18 Trans.	1.35	2.41
2nd BSW18 Refl.	0.977	3.81
2nd BSW18 Trans.	1.37	2.34
Extra BSW18 Refl.	1.02	3.62
Extra BSW18 Trans	1.27	2.67
NENIR201B	1.95	0.821
NENIR203D	1.14	3.15
NENIR205B	0.792	4.72
NENIR213B	0.120	12.9
NENIR240B*	-	37.0

*Value taken from Thorlabs raw data sheet [53].

A.2 Additional Long-Fiber Pulse-Shape Comparisons

Fig. A.1 shows four additional normalized pulse-shape comparisons from the 17.7 dB baseline attenuation measurement using the long fiber. The figure provides supplementary examples of the transmitted pulse distortion discussed in Section 4.3.

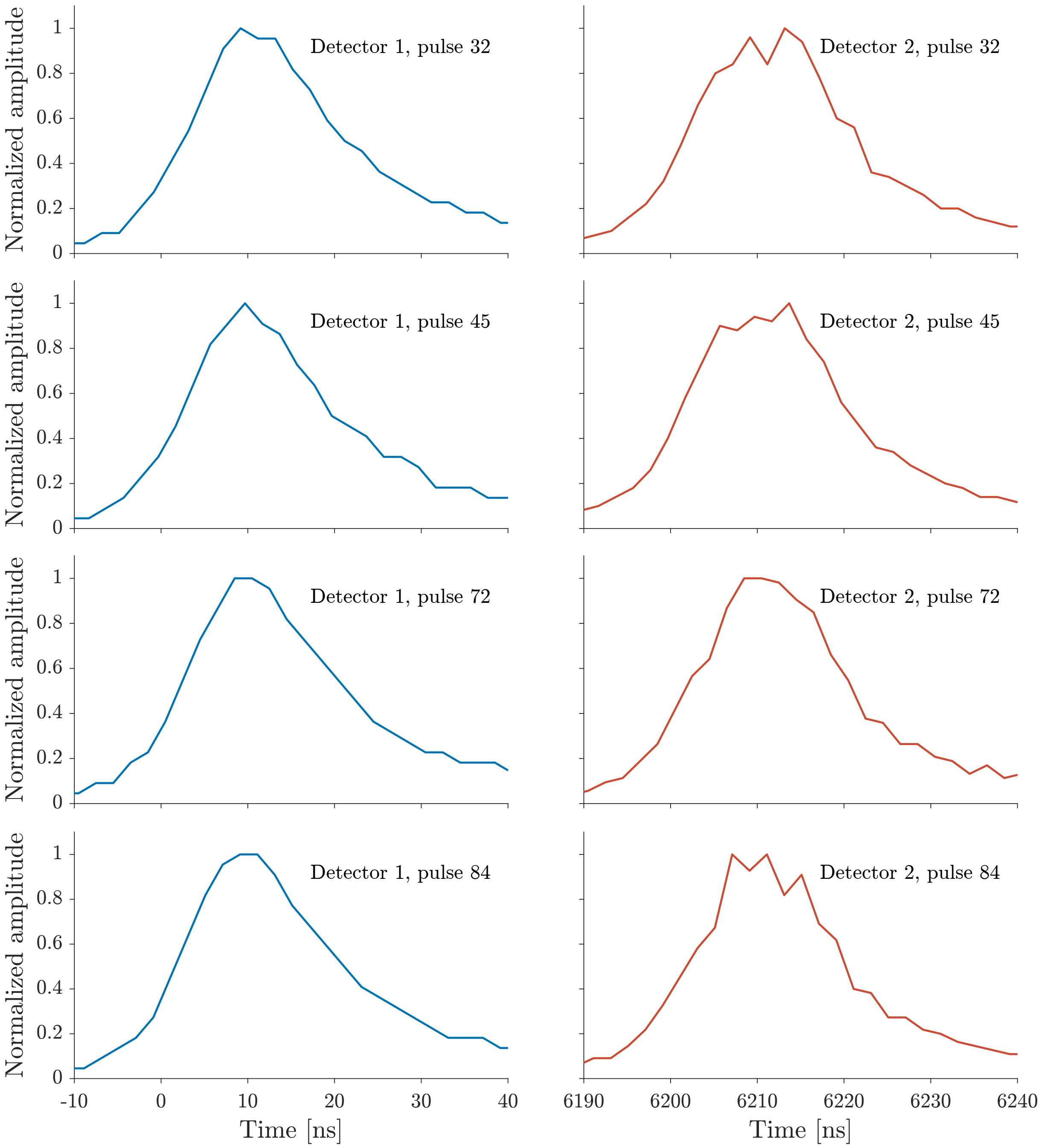

Figure A.1: Extended comparison of temporal pulse shapes for four representative pulses from the 17.7 dB baseline attenuation measurement using the long fiber. The left panels show the incident detector pulses in blue before fiber propagation, while the right panels show the corresponding pulses after propagation through the fiber in red. Each row corresponds to one selected pulse.

DEPARTMENT OF MICROTECHNOLOGY AND NANOSCIENCE
CHALMERS UNIVERSITY OF TECHNOLOGY
Gothenburg, Sweden
www.chalmers.se

CHALMERS
UNIVERSITY OF TECHNOLOGY